

This item is likely protected under Title 17 of the U.S. Copyright Law. Unless on a Creative Commons license, for uses protected by Copyright Law, contact the copyright holder or the author.

Access to this work was provided by the University of Maryland, Baltimore County (UMBC) ScholarWorks@UMBC digital repository on the Maryland Shared Open Access (MD-SOAR) platform.

Please provide feedback

Please support the ScholarWorks@UMBC repository by emailing scholarworks-group@umbc.edu and telling us what having access to this work means to you and why it's important to you. Thank you.

CORONA, JET, AND RELATIVISTIC LINE MODELS FOR *SUZAKU*/*RXTE*/*CHANDRA*-HETG OBSERVATIONS OF THE CYGNUS X-1 HARD STATE

MICHAEL A. NOWAK¹, MANFRED HANKE², SARAH N. TROWBRIDGE¹, SERA B. MARKOFF³, JÖRN WILMS², KATJA POTTSCHMIDT⁴,
 PAOLO COPPI⁵, DIPANKAR MAITRA^{3,6}, JOHN E. DAVIS¹, AND FRANK TRAMPER³

¹ Massachusetts Institute of Technology, Kavli Institute for Astrophysics, Cambridge, MA 02139, USA;
mnowak@space.mit.edu, davis@space.mit.edu, saraht@mit.edu

² Dr. Karl Remeis-Sternwarte and Erlangen Centre for Astroparticle Physics, Universität Erlangen-Nürnberg, Sternwartstr. 7, 96049 Bamberg, Germany;
Manfred.Hanke@sternwarte.uni-erlangen.de, joern.wilms@sternwarte.uni-erlangen.de

³ Astronomical Institute “Anton Pannekoek” University of Amsterdam, The Netherlands; s.b.markoff@uva.nl, dmaitra@umich.edu

⁴ CRESST, UMBC, and NASA Goddard Space Flight Center, Greenbelt, MD 20771, USA; katja@milkyway.gsfc.nasa.gov

⁵ Yale University, New Haven, CT, USA; paolo.coppi@yale.edu

Received 2010 February 18; accepted 2010 November 24; published 2011 January 14

ABSTRACT

Using *Suzaku* and the *Rossi X-ray Timing Explorer* (*RXTE*), we have conducted a series of four simultaneous observations of the galactic black hole candidate Cyg X-1 in what were historically faint and spectrally hard “low states.” Additionally, all of these observations occurred near superior conjunction with our line of sight to the X-ray source passing through the dense phases of the “focused wind” from the mass donating secondary. One of our observations was also simultaneous with observations by the *Chandra*-High Energy Transmission Grating (HETG). These latter spectra are crucial for revealing the ionized absorption due to the secondary’s focused wind. Such absorption is present and must be accounted for in all four spectra. These simultaneous data give an unprecedented view of the 0.8–300 keV spectrum of Cyg X-1, and hence bear upon both corona and X-ray emitting jet models of black hole hard states. Three models fit the spectra well: coronae with thermal or mixed thermal/non-thermal electron populations and jets. All three models require a soft component that we fit with a low temperature disk spectrum with an inner radius of only a few tens of GM/c^2 . All three models also agree that the known spectral break at 10 keV is not solely due to the presence of reflection, but each gives a different underlying explanation for the augmentation of this break. Thus, whereas all three models require that there is a relativistically broadened Fe line, the strength and inner radius of such a line is dependent upon the specific model, thus making premature line-based estimates of the black hole spin in the Cyg X-1 system. We look at the relativistic line in detail, accounting for the narrow Fe emission and ionized absorption detected by HETG. Although the specific relativistic parameters of the line are continuum dependent, none of the broad line fits allow for an inner disk radius that is $>40 GM/c^2$.

Key words: accretion, accretion disks – black hole physics – radiation mechanisms: non-thermal – X-rays: binaries

Online-only material: color figures

1. INTRODUCTION

There is currently significant debate as to the physical mechanisms responsible for the continuum of X-ray spectrally “hard states” of black hole candidates (BHCs) accreting in binaries. This debate ranges from the broader issue of whether or not there is a significant contribution to the X-ray band from an outflow or jet, to more narrowly focused issues within given classes of models. For instance, the hard X-ray emission has traditionally been attributed to a Comptonizing thermal corona (Eardley et al. 1975; Shapiro et al. 1976; Sunyaev & Trümper 1979; Dove et al. 1998, and references therein). These earlier works generally favor a scenario where the corona lies central to a truncated outer thin disk. However, if the corona is driven outward by radiative pressure (e.g., Beloborodov 1999) could it instead overlay the inner disk? Can the optically thick, geometrically thin disk extend inward nearly to the innermost stable circular orbit (ISCO; Miller et al. 2006)? Is this disk cold (peak temperatures of a few hundred eV), or can it instead be hot (near a keV, i.e., Wilms et al. 2006)? Is the hard state corona comprised primarily of electrons with a thermal

population (Poutanen & Vurm 2009), or can it have a substantial contribution from a non-thermal electron population (Ibragimov et al. 2005)? Does the bulk motion of the flow play a role in Comptonizing the spectrum (Shaposhnikov & Titarchuk 2006; Laurent & Titarchuk 2007)? Alternatively could the X-rays be comprised of a combination of direct synchrotron and synchrotron self-Compton (SSC) emission from a jet (Markoff et al. 2005; Maitra et al. 2009)? Contributing to the debate, however, is the fact that many of the above cited models, especially when considering solely *Rossi X-ray Timing Explorer* (*RXTE*) data in the 3–200 keV range (or even narrower energy ranges), describe the hard state spectra nearly equally well.

To study these issues, over the past decade we have been using a series of pointed, approximately bi-weekly, *RXTE* observations of the BHC Cyg X-1 performed simultaneously with 15 GHz radio observations by the Ryle telescope. Cyg X-1 holds much promise for exploring the current range of questions listed above owing to its persistently bright X-ray flux (including both the hard and soft states, it varies between 200 and 600 mCrab in the 1.2–12 keV band covered by the *RXTE*-All Sky Monitor (ASM)) and its correlated radio/X-ray spectra (see Wilms et al. 2006, and references therein). Extended radio emission even has been imaged in Cyg X-1 (Stirling et al. 2001). This campaign has already provided the spectra for some of the

⁶ Current address: Department of Astronomy, University of Michigan, 500 Church St., Ann Arbor, MI 48109-1042, USA.

Comptonization models (Wilms et al. 2006) and jet models (Markoff et al. 2005) discussed above. Additionally, these data have been used to study the correlation of the X-ray and radio spectral properties on both long timescales (Pottschmidt et al. 2000, 2003; Wilms et al. 2006) and short timescales (Gleissner et al. 2004a; Wilms et al. 2007; Böck et al. 2010; M. Böck et al. 2011, in preparation). Thus, they comprise a strong data set for addressing not only the details of the X-ray spectrum, but also the connection to the hard state jets which are known to dominate the radio through near-infrared emission. Simultaneous radio/X-ray flaring has also been detected in Cyg X-1 during this extended campaign (Fender et al. 2006; Wilms et al. 2007), lending support to the hypothesis of X-ray emission by the jet.

RXTE spectral data alone, however, do not allow us to break the current existing “theoretical degeneracy” in the origin of the X-ray spectrum. The statistically best fits are in fact obtained with purely empirical simple broken power laws with a break occurring between 9 and 12 keV, and an exponential cutoff occurring at >20 keV, to which a broad, ≈ 6.4 keV Gaussian line is added (Wilms et al. 2006; Nowak et al. 2005). The latter component is likely attributable to a relativistically broadened Fe $K\alpha$ line (Reynolds & Nowak 2003, and references therein); however, its parameters are dependent upon the assumed continuum model (Wilms et al. 2006). More physically motivated Comptonization and outflow-dominated models (Markoff et al. 2005; Wilms et al. 2006) can describe the same spectra almost as well. However, they must introduce additional, albeit plausible, physical components (e.g., relativistic smearing) to recover the simple spectra of the broken power-law description. Thus, there is some amount of ambiguity when correlating detailed spectral features versus continuum properties, e.g., disk reflection versus coronal compactness/hardness, as the detailed features systematically depend upon the underlying broadband continuum.

Despite these problems in finding a truly unique spectral model, when considering multiple observations taken over a wide range of luminosities and spectral hardnesses, spectral correlations arise that are robust and persistent across a variety of these theoretical characterizations (Wilms et al. 2006). Using the broken power-law models as a simple description of the X-ray spectra, we have found that when the 2–10 keV photon index $\Gamma_1 < 2.2$ there is a positive correlation between X-ray and radio flux, whereas for $\Gamma_1 > 2.2$ there is a negative correlation between the X-ray and radio flux. We therefore use the value of $\Gamma_1 \approx 2.2$ as the canonical division between the spectrally “hard state” and the spectrally “soft state” (see Remillard & McClintock 2006). Additionally, as the spectra become harder, exponential cutoffs tend to become less significant (see also Motta et al. 2009).

Our previous *RXTE* spectral studies of Cyg X-1 have been limited in two respects: the low spectral resolution of *RXTE* ($E/\Delta E \approx 6$ at 6 keV) and the inability to measure spectra at $\lesssim 3$ keV. In this work, we turn to a set of four *Suzaku* observations that we performed simultaneously with our *RXTE* campaign to enhance our Cyg X-1 studies in several crucial ways. First, *Suzaku* has large effective area at soft X-ray energies. In this work, we consider spectra down to 0.8 keV, which allows for the possibility of measuring the “seed photon spectrum” in Comptonization models (Section 5.1), or judging the relative contribution of synchrotron versus the disk radiation in jet models (Section 5.2). *Suzaku* also has excellent resolution in the Fe $K\alpha$ line region ($E/\Delta E \approx 50$), which allows us to separate narrow from relativistically broadened line features

(Sections 4.3 and 5.3). Third, *Suzaku* measures the Cyg X-1 hard X-ray spectrum up to ≈ 300 keV (Section 4.1), providing further constraints on Comptonization and jet models.

The outline of this paper is as follows. In Section 2, we describe our full set of observations and our data reduction procedures. Due to maintenance and upgrade of the Ryle radio telescope during the construction of the Arcminute Microkelvin Imager, no simultaneous radio measurements are available for these *Suzaku/RXTE* observations. Instead, we use previous observations to estimate the radio fluxes (Section 2.4). For one of our observations simultaneous *Chandra*-High Energy Transmission Grating (HETG) data are available (Section 2.3). These *Chandra* data become crucial in all of our analyses as they help elucidate the spectral variability associated with the observed light curve behavior, as discussed in Section 3. We present simple phenomenological descriptions of the spectra in Section 4, including a description of the composite line profile (Section 4.3). Comptonization and jet models are presented in Section 5, along with further discussions of the implied relativistic lines (Section 5.3). We summarize our findings in Section 6.

2. OBSERVATIONS AND DATA ANALYSIS

Prior to 2009 April, there have been five *Suzaku* observations of Cyg X-1. The four most recent of these observations are discussed in this work. The first *Suzaku* Cyg X-1 observation occurred in 2005 October (Makishima et al. 2008). During this observation Cyg X-1 was in a relatively bright hard state (the *RXTE*-ASM count rate was ≈ 30 count s^{-1}), the spacecraft aim-point was placed on the *Suzaku* X-ray Imaging Spectrometer (XIS) detectors, and *Suzaku* was run in a data mode with 1 s integrations per CCD exposure frame. As discussed by Makishima et al. (2008; see also the Appendix), this long exposure led to both telemetry dropouts and severe photon pileup on the detectors. As these issues require a more complex analysis (Makishima et al. 2008), we do not consider these data further.

The four *Suzaku* observations discussed here occurred during times when the *RXTE*-ASM flux ranged from 12 to 23 count s^{-1} , the spacecraft pointing was set to the hard X-ray detector (HXD; this slightly reduces the flux on the XIS detectors), and the CCD exposure frame integration times were set to ≈ 0.5 s. Thus, our observations do not suffer from telemetry dropouts and they are less severely affected by photon pileup. All four of these observations occurred simultaneously with *RXTE* observations. The last of these observations also occurred simultaneously with observations by every other X-ray/soft gamma-ray instrument flying at that time (M. Hanke et al. 2011, in preparation). Here, we only consider the simultaneous *Chandra*-HETG data. An observing log is presented in Table 1.

2.1. *Suzaku* Analysis

The *Suzaku* data were reduced with tools from the HEASOFT v6.8 package and calibration files dated 2009 September 25. The instruments on *Suzaku* (Mitsuda et al. 2007) are the XIS (Koyama et al. 2007) CCD detector covering the ≈ 0.3 –10 keV band, and the Hard X-ray Detector (HRD; Takahashi et al. 2007) comprised of the PIN diode detector (PIN) covering the ≈ 10 –70 keV band and the gadolinium silicate crystal detector (GSO) covering the ≈ 60 –600 keV band. The XIS has four separate detectors, XIS 0–3, with XIS 1 being a backside

Table 1
Log of Cyg X-1 Observations

Date (yyyy-mm-dd)	Spacecraft/ObsID	Instrument	Exposure (ks)	
2006-10-30	<i>Suzaku</i> /401059010	XIS 0–3	35.0 ^a	32.1
...	...	HXD-PIN	27.7	24.9
...	...	HXD-GSO	27.7	25.8
...	<i>RXTE</i> /80110-01-13	PCA	8.0 ^b	8.0
...	...	HEXTE-A	3.1	3.1
...	...	HEXTE-B	2.5	2.5
2007-04-30	<i>Suzaku</i> /402072010	XIS 0,1,3	34.0 ^a	22.4
...	...	HXD-PIN	40.2	27.6
...	...	HXD-GSO	40.2	27.1
...	<i>RXTE</i> /92090-01-16	PCA	14.6 ^b	1.5
...	...	HEXTE-A	4.6 ^{c,d}	0.3
...	...	HEXTE-B	3.0	0.4
2007-05-17	<i>Suzaku</i> /402072020	XIS 0,1,3	22.3 ^a	12.3
...	...	HXD-PIN	32.6	10.9
...	...	HXD-GSO	32.6	10.9
...	<i>RXTE</i> /92090-01-17	PCA	2.0 ^b	0.0
...	...	HEXTE-A	1.9 ^{c,d}	0.0
...	...	HEXTE-B	0.9	0.0
2008-04-19	<i>Suzaku</i> /403065010	XIS 1,3	16.9 ^a	7.2
...	...	XIS 0	34.0 ^e	0.0
...	...	HXD-PIN	29.0	10.1
...	...	HXD-GSO	29.0	10.1
...	<i>RXTE</i> /93120-01-01	PCA	21.5 ^b	7.2
...	...	HEXTE-A	17.9 ^c	7.1
...	...	HEXTE-B	10.8	4.6
...	<i>Chandra</i> /8525	HETG	29.4 ^f	11.1 ^g

Notes. Exposure times are after initial good time filtering (left) and after color/intensity time filtering (right).

^a Summed exposure times for all listed XIS detectors.

^b Summed exposure intervals, not weighted by the fraction of operating Proportional Counter Units (PCU).

^c HEXTE-A cluster in fixed position (no rocking).

^d Evidence for HEXTE-A cluster exposure time anomaly.

^e XIS 0 run in continuous readout mode.

^f Summed exposure times for all first-order spectra.

^g Summed exposure times for first-order HEG spectra.

illuminated CCD. XIS 2 was lost due to a micrometer hit in late 2006, and thus was available only for the first observation (see Table 1). For our fourth observation, XIS 0 was run in continuous readout mode, which is not yet fully calibrated, so we do not include these data in this work.

In preparing the XIS spectra, we first corrected each detector for charge transfer inefficiency using the `xispi` tool, and then reprocessed the data with `xselect` using the standard `xisrepro` selection criteria. Due to thermal flexing of the spacecraft, the attitude of the *Suzaku* spacecraft exhibits variability over the course of the observations and therefore the image of the source is not at a fixed position on the CCD. Standard processing reduces this variability and improves the point spread function (PSF) image (Uchiyama et al. 2008); however, with the standard tools it is not possible yet to correct fully the blurring caused by the varying attitude. As described in the Appendix, for bright sources a better reconstruction of the attitude solution, and thus narrower PSF images, can be obtained using the `aeattcor.sl` software. We produced such an improved image and then used the `pile_estimate.sl` S-Lang script described in the Appendix to estimate the degree of pileup in the observations. For the spectra described in this work, using the time filter criteria described in Section 3, the center of the PSF images could be affected by as much as a 35% pileup fraction.

We therefore extracted annular regions wherein we excised the $\approx 20''$ radius central region. The excised data accounted for approximately 1/3 of the detected events. The outer radii of our annular extraction regions were limited by the 1/4 sub-array used in our CCD readout mode, and thus were $\approx 2'$. We estimate that the extracted events had $<4\%$ mean residual pileup fraction. All regions of the CCD are dominated by source counts, therefore we did not extract nor use any background spectra for the XIS observations.

Events in the XIS detectors were read out from either 3×3 or 2×2 pixel islands. The XIS 1 data were always in 3×3 mode, whereas the other detectors had mixtures of 3×3 and 2×2 mode. We created individual spectra and response files for each detector and data mode combination. Spectra were created for the time intervals described in Section 3, with the resulting exposure times also being listed in Table 1. Response matrices and effective area files were created with the `xismfgen` and `xissimarfgen` tools, respectively.

Although for each observation the individual XIS spectra were fit separately, they were jointly grouped on a common grid such that they had a minimum combined signal-to-noise ratio of 8 in each energy bin (i.e., 64 total counts in each bin) and that the minimum number of channels per energy bin was at least the half-width half-maximum of the spectral resolution.⁷ To avoid regions of poorly understood response, we only considered spectral energy ranges 0.8–1.72 keV, 1.88–2.19 keV, and 2.37–7.5 keV.⁸

For the PIN, we extracted spectra from the “cleaned” event files in the `hxd/event_c1` directories. The appropriate response and background files were downloaded from the High Energy Astrophysics Science Archive Research Center (HEASARC), specifically those from the `pinxb_ver2.0_tuned` directory. Good time intervals (GTIs) were merged from our time selections (Section 3) and the combination of the GTI intervals from the source and background event files. These intersected intervals were then used to extract the PIN source and background spectra. The source spectra exposure times were then corrected with the `hxdcorr` tool. The PIN spectra were grouped to have a signal-to-noise ratio ≥ 10 in each energy bin, and we considered spectra between 12 and 70 keV.

The GSO spectra were created starting with the “unfiltered” event files. These data were first reprocessed with the `hxdtime`, `hxdpi`, and `hxdgrade` tools, following the “*Suzaku ABC Guide*.” The data were then filtered in `xselect` with the standard criteria from the HEASARC provided `gso_mkf.sel` script. The background was downloaded from the `gsonxb_ver2.0` directory at HEASARC. GTI from the event file, the background file, and the time intervals were merged, and spectra were extracted from these times. Response files were then taken from the CALDB database, and exposure times were adjusted to agree with the spectra. The grouping of the GSO spectra is essentially fixed by the grouping of the background file, thus no rebinning was performed on these spectra. It was determined that the background

⁷ The half-width half-maximum (HWHM) was determined by using the spectral responses to create fake spectra of delta function lines at discrete energies. These fake spectra were then fit without response matrices to determine HWHM. In practice, this meant that the original spectra with 4096 channels each were grouped, using the `ISIS` group function, by a minimum of 6, 8, 12, 14, 16, 18, 20, and 22 channels starting at 0.5, 1, 2, 3, 4, 5, 6, and 7 keV, respectively. For the most part, the spectral binnings were dominated by the HWHM criteria rather than the signal-to-noise criterion.

⁸ Outside of these energy ranges there are large disagreements among the fit residuals for the individual detectors and data modes. The excised regions between 1.72 and 2.37 keV correspond to poorly calibrated Si and Ir features related to the detectors and mirrors.

becomes prohibitive above 300 keV; therefore, we restrict the GSO spectra to the 60–300 keV range.

2.2. *RXTE* Analysis

The *RXTE* data were prepared with tools from the HEASOFT v6.8 package and the most current calibration files as of 2010 January 10. We used standard filtering criteria for data from the Proportional Counter Array (PCA; Jahoda et al. 1996). Specifically, we excluded data from within 30 minutes of South Atlantic Anomaly passage, from whenever the target elevation above the limb of the earth was less than 10° , and from whenever the electron ratio (a measure of the charged particle background) was greater than 0.15. We used the background models appropriate to bright data.

We applied 0.5% systematic errors to all PCA channels, added in quadrature to the errors calculated from the data count rate. For all PCA fits we grouped the data starting at ≥ 3 keV with the criteria that the signal to noise (after background subtraction, but excluding systematic errors) in each bin had to be ≥ 4.5 . We restricted the noticed energy range to 3–22 keV.

We extracted data from the High Energy X-ray Timing Experiment (HEXTE; Rothschild et al. 1998) using the same criteria as for the PCA. HEXTE is comprised of two clusters, A and B. Prior to 2007, both clusters were in a rocking mode, with only one detector viewing the source at a given time, while the other detector conducted off-source background measurements. For later dates (e.g., our three most recent observations), HEXTE A has been in a fixed on-source position, which required us to estimate cluster A backgrounds using the `hextebackest` tool. Furthermore, during our third observation there was clear evidence for a HEXTE A exposure anomaly.⁹ We found evidence for such an anomaly (albeit less severe) in our second observation as well. We corrected the HEXTE A exposure time by iteratively fitting an exponentially cutoff power law simultaneously to both cluster A and B data and varying the exposure of cluster A until a χ^2 minimum was achieved using the same normalization for both detectors.

We binned the HEXTE spectra to a common grid such that they had a minimum combined signal to noise of eight in each energy channel (even though both clusters were fit individually). We further restricted the noticed energy range to 18–200 keV. Additionally, when fitting the X-ray spectra we allowed the normalization of the HEXTE backgrounds to vary. (The best-fit normalization constants were typically within $\lesssim 10\%$ of unity.)

For both PCA and HEXTE spectra, we further restricted the considered time intervals to those that were strictly simultaneous with the *Suzaku* spectra. That is, the *RXTE* time intervals form a subset of the *Suzaku* time intervals.

2.3. *Chandra*-HETG Analysis

The HETG (Canizares et al. 2005) was inserted for our observation of Cyg X-1, with the data readout mode being Timed Exposure-Graded. The HETG is comprised of the High Energy Gratings (HEGs), with coverage from ≈ 0.7 –8 keV, and the Medium Energy Gratings (MEGs), with coverage from ≈ 0.4 –8 keV. To minimize pileup in the gratings spectra, a 1/2 subarray was applied to the CCDs. Additionally, the observatory aimpoint was placed closer to the CCD readout. This configuration reduces the frame time to 1.741 s, without any loss of the dispersed spectrum.

We used CIAO v4.2 and CALDB v4.2.0 to extract the data and create the spectral response files. The location of the center of the zeroth-order image was determined using the `findzo.sl` routine,¹⁰ which provides ≈ 0.1 pixel (≈ 0.001 Å, for MEG) accuracy. The data were reprocessed with pixel randomization turned off, but PHA randomization left on. We applied the standard grade and bad pixel file filters, but we did not destreak the data.

Although the instrumental set up was designed to minimize pileup, it is still present in both the MEG and, to a lesser extent, the HEG spectra. We incorporate the effects of pileup in our spectral fits using the `simple_gpil2` model (Hanke et al. 2009) based upon the model originally described by Nowak et al. (2008). For the small amount of pileup present in these data, this model is extremely successful in describing its effect on the spectra.

As for the PCA and HEXTE spectra, we restricted the considered time intervals for the *Chandra* spectra to those that were strictly simultaneous with the *Suzaku* spectra.

2.4. Estimated Radio Fluxes

Simultaneous Ryle radio fluxes are not available for the X-ray observations discussed in this work. Owing to the known stringent correlations between the X-ray and radio flux, specifically the correlations between the *RXTE*-ASM and Ryle fluxes (see Gleissner et al. 2004b; Nowak et al. 2005), we use an estimated radio flux when applying the jet model to the spectra (Section 5.2). From our prior observations, we average all radio data that occurred at times with ASM daily averages that were within $\pm 1\sigma$ of the ASM daily average corresponding to these new observations. The average and standard deviation of these radio data were used in the spectral fits, which yielded radio fluxes of 12.6 ± 3.3 mJy (2006 October 30), 10.8 ± 3.9 mJy (2007 April 30), 7.9 ± 3.0 mJy (2007 May 17), and 10.2 ± 3.0 mJy (2008 April 19). Each average was comprised of a minimum of 10 measurements, and the extreme radio flux values within each sample never differed from the average by more than a factor of two.

2.5. Data Plots

Throughout this work we will present spectra that are “unfolded” from the detector response in a model-independent manner (see Nowak et al. 2005). Specifically, we define the unfolded photon flux, $F_{\text{unfold}}(h)$, from a pulse height (PHA) bin, h , as

$$F_{\text{unfold}}(h) = \frac{C(h) - B(h)}{\int R(h, E) A(E) dE \Delta t}, \quad (1)$$

where $C(h) - B(h)$ are the background subtracted counts, $R(h, E)$ and $A(E)$ are the detector response matrix and effective area, and Δt is the exposure time. For multiple data sets co-added together for the plots (e.g., the *Suzaku*-XIS or the *RXTE*-HEXTE data), the numerator and denominator are each replaced with the sum of the same quantities from the detectors. Throughout we only sum data for the plots, not for the fits.

Model spectra are “unfolded” in a similar manner. That is, predicted background subtracted model counts are first calculated, and then unfolded as above. Thus, the model spectra exhibit the smearing induced by the detector response matrix. The one exception to this model component scheme is for the jet results presented in Section 5.2. There some of the model

⁹ http://gsfc.nasa.gov/docs/xte/whatsnew/newsarchive_2007.html

¹⁰ <http://space.mit.edu/ASC/analysis/findzo/>

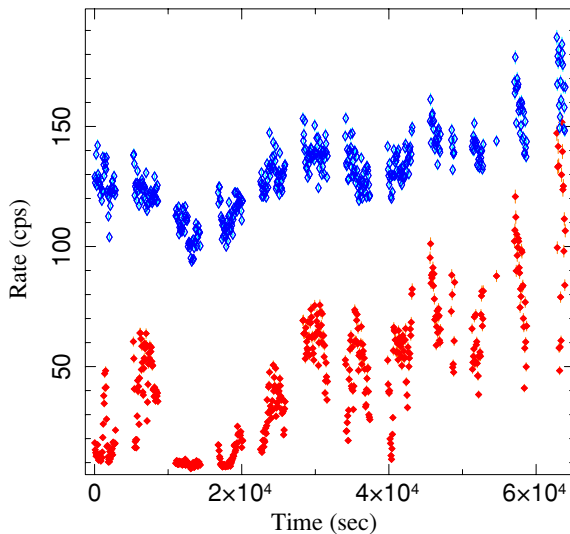


Figure 1. *Suzaku*-XIS 1 light curves (16 s integration bins) for observation 4 in the 0.5–1.5 keV band (filled diamonds, bottom curve) and the 3–9 keV band (hollow diamonds, top curve, shifted upward by 50 count s⁻¹).

(A color version of this figure is available in the online journal.)

components are shown unsmoothed by the detector response, as they are derived from internal calculations of the jet code.

3. LIGHT CURVES

By design, our fourth observation occurred near binary orbital phase 0 (superior conjunction of the black hole), wherein we expected to be viewing Cygnus X-1 through the wind of the secondary. By happenstance, all of our remaining *Suzaku* observations also occurred near superior conjunction, i.e., observations 1–4 cover orbital phases 0.2–0.3, 0.8–0.0, 0.85–0.0, and 0.0–0.14, respectively. Although dipping events are known to be present during all orbital phases, during upper conjunction dipping is prevalent due to absorption by clumps in the wind (Bałucińska-Church et al. 2000). This behavior is clearly seen in the *Suzaku* light curves presented in Figure 1. The soft X-ray light curve shows a deep, prolonged ≈ 12 ks dip. A less pronounced, but still significant dip is seen in the hard X-ray light curve (Hanke et al. 2008). Numerous dips of varying levels are also seen on even shorter timescales. In order to extract the unabsorbed spectrum of the source, it is therefore necessary to screen the data for dipping and excise the dipping intervals from further analysis.

In addition to dipping, spectral modeling also has to take into account the strong dust scattering halo in front of Cyg X-1 (Predehl & Schmitt 1995). As discussed by Xu et al. (1986, and references therein), a scattering halo is produced by the scattering of radiation from an X-ray source by a foreground dust cloud. Typical halo sizes are on the order of arcminutes, i.e., comparable to the size of the *Suzaku* PSF. The energy dependence of the scattering cross section leads to a halo angular size that is $\propto E^{-1}$ and a halo spectrum that is $\propto E^{-2}$. Furthermore, as the scattered photons travel along a greater path length to reach the observer, they are delayed with respect to the directly observed photons by a factor that is proportional to the square of the angular radius from which the scattered photons are observed. The expected time delays for nearby galactic sources typically range from thousands to tens of thousands of seconds.

Thus, the *Suzaku* spectrum and light curve of Cyg X-1 are comprised of two components: a directly observed component, subject to the local dipping events, and a time-delayed and time-

averaged (due to integration over different angular radii) softer spectrum from the scattering halo. Most spectral analyses in the past have ignored the effects of scattering since to first order for optically thin scattering in a homogeneous cloud, whatever radiation that is scattered out of the line of sight is scattered back in from larger (often spatially unresolved) radii. Thus, for spatially unresolved (on the size scale of the halo) and steady sources, dust can be ignored in simple analyses.

If one assumes that the time-delayed and time-averaged spectrum is represented by the same model as the direct spectrum, and if one further assumes that interstellar absorption is predominantly in the foreground of the dust halo, within ISIS one can write the spectral model for the spectra during the dips as

$$\text{TBnew}(1) * (1 - \text{dustscat} * (1 - \text{TBnew}(2))) * (\text{continuummodel}). \quad (2)$$

Here and throughout we shall use an updated version¹¹ of the absorption model of Wilms et al. (2000) to describe both the interstellar (model instance 1) and local (model instance 2) absorption. The *dustscat* model is a version of the XSPEC dust model that removes the optically thin assumption of the latter model, but otherwise ignores multiple scatterings (F. Baganoff 2007, private communication). Note that when local absorption is absent ($\text{TBnew}(2) \rightarrow 1$), the dust scattering term drops out of the model expression.

Not all of the assumptions encompassed within the above model expression are necessarily realistic. Specifically, the assumptions that all interstellar absorption is foreground to the dust and that the delayed source spectrum is identical to direct spectrum are undoubtedly wrong in fine detail. However, we find that the above expression provides a reasonable description of the color–color diagrams in Figure 2. Specifically, we create a spectrum from bright phases of the light curve that inhabit a locus of points in the upper right-hand corner of the color–color diagrams (i.e., the filled symbols of Figure 2). We fit a simple spectral model to these selected data: an absorbed disk plus power law plus broad and narrow Gaussian lines near 6.4 keV. We then apply this model in Equation (2) and create color–color curves by varying the *TBnew*(2) component from 0 to $2 \times 10^{23} \text{ cm}^{-2}$. These curves are then fit to the color–color diagrams using the optical depth of the dust scattering halo as the single free parameter. Our best fits yield $\tau = 0.24\text{--}0.34$, and the results are shown in Figure 2.

Overall, these curves describe the behavior of the color–color diagrams reasonably well. The dust halo represents $\approx 20\%\text{--}30\%$ (i.e., on the order of the scattering optical depth) of the soft X-ray ($\lesssim 2$ keV) flux being “uncovered” during the dips. Given the much narrower *Chandra* PSF, one would expect comparable *Chandra* color–color diagrams to show a far smaller uncovered fraction if the dust halo interpretation is correct. This is indeed found to be true, with *Chandra* showing only an $\approx 2\%$ uncovered fraction (Hanke et al. 2008; M. Hanke et al. 2011, in preparation). However, it is possible that the very low uncovered fraction required by the *Chandra* data might, in fact, be partly intrinsic to the local dipping at the source (M. Hanke et al. 2011, in preparation). Note that the theoretical curves show a greater degree of curvature than the observed, nearly linear, evolution toward the lower left-hand corner of the diagram. We hypothesize that this discrepancy is due to

¹¹ <http://pulsar.sternwarte.uni-erlangen.de/wilms/research/tbabs/>

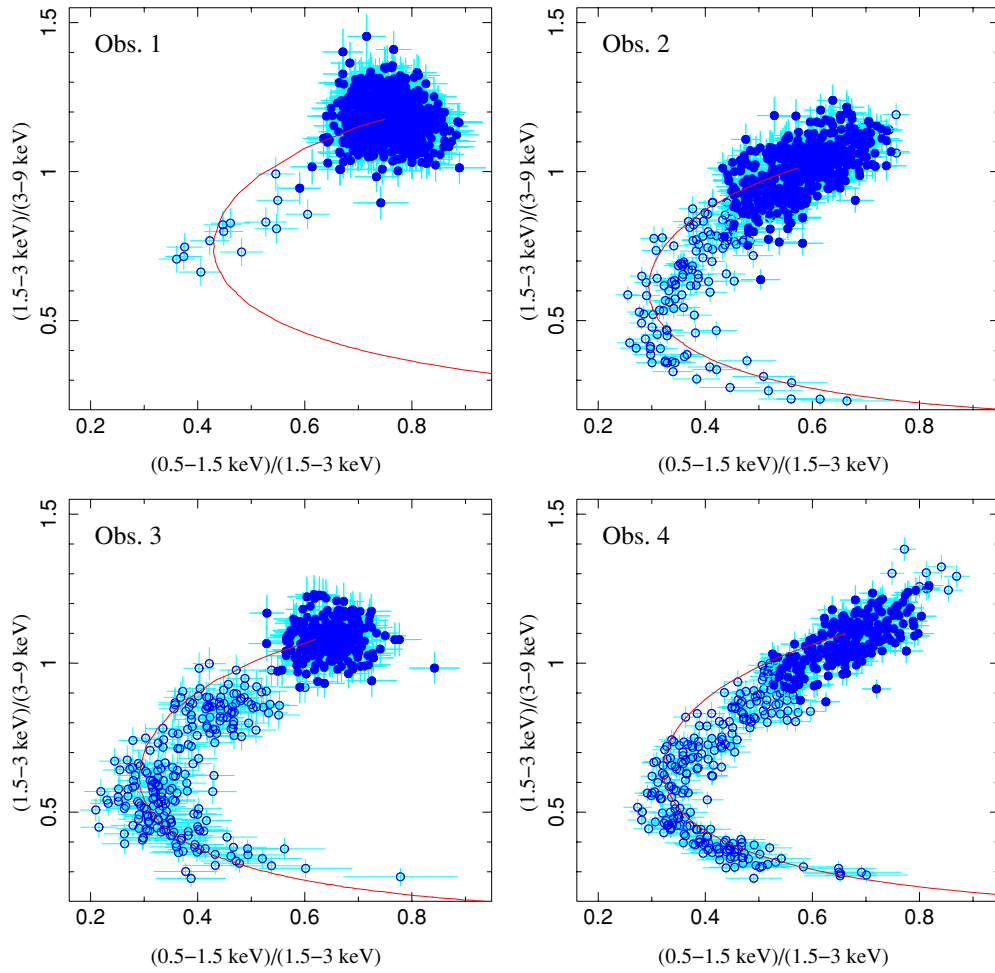


Figure 2. *Suzaku*-XIS 1 color-color diagrams, made with 16 s bins. The colors are created from the count rate in three bands: 0.5–1.5 keV, 1.5–3 keV, and 3–9 keV. The lines are the best fit dust halo models, presuming that the source is obscured by both an interstellar neutral column as well as by a neutral column local to the source, with the latter ranging in value from $0\text{--}2 \times 10^{23} \text{ cm}^{-2}$. Filled symbols indicate the periods used for the spectral analyses described in this work (see the text). (A color version of this figure is available in the online journal.)

our assumption in Equation (2) of purely neutral absorption in the dips. A concurrent increase in the optical depth of ionized absorption could serve to alter the theoretical curves in the appropriate manner. We return to this concept of an ionized absorber component in Section 4.2.

4. SIMPLE SPECTRAL MODELS

The light curves and color-color diagrams described above were used to create spectra for the time periods corresponding to the bright phases of the light curve represented in the upper right corner of the color-color diagrams (Figure 2). The selections that we made are highlighted as filled symbols within these figures. The resulting exposure times are given in Table 1. With the exception of the *RXTE*-only broken power-law spectral fits described immediately below, throughout the rest of this work we shall only describe spectra from these bright phase, minimally locally absorbed time periods.

4.1. Broken and Cutoff Power-law Descriptions

As discussed by Wilms et al. (2006), nearly all *RXTE*-PCA and *HEXTE* spectra of Cyg X-1 can be described by an *extremely* simple phenomenological model: an absorbed, exponentially cutoff, broken power law plus a broad, Gaussian line. The photon indices of the broken power law, which we label as Γ_1 and Γ_2

for the soft ($\approx 3\text{--}10$ keV) and hard ($\gtrsim 10$ keV) X-rays, show a correlation in the sense that the amplitude of the break between the two, $\Gamma_1 - \Gamma_2$, increases with higher (i.e., softer) values of Γ_1 . This $\Gamma\text{--}\Delta\Gamma$ correlation is a very phenomenological description of the spectral correlation that elsewhere has been described as a “ $\Gamma\text{--}\Omega/2\pi$ ” (hardness/reflection fraction) correlation (Zdziarski et al. 1999). Following Remillard & McClintock (2006), Wilms et al. (2006) classified spectra with $\Gamma_1 \lesssim 2.2$ as “hard state” spectra.

In order to compare the spectra discussed here to the work of Wilms et al. (2006), we take the nine *RXTE* spectra¹² and fit them with exponentially cutoff broken power laws. As in the work of Wilms et al. (2006), these simple phenomenological models are excellent descriptions of these data. This is even true for the spectra extracted from times of moderate and deep dips. These latter spectra have slightly reduced values of Γ_1 and increased values of the fitted neutral column, N_H (Wilms et al. 2006 show that orbital phase dependence of the column is discernible in our *RXTE* observations of Cyg X-1), but otherwise appear similar to non-dip phase spectra. This is not entirely surprising given that *RXTE* is primarily sensitive at energies $\gtrsim 3$ keV, and therefore

¹² These nine spectra consist of three bright phase spectra and six spectra taken from deeper dipping periods. Observation 1 shows no strong dips and observation 3 does not have *RXTE* data strictly simultaneous with the bright phases of the *Suzaku* spectra.

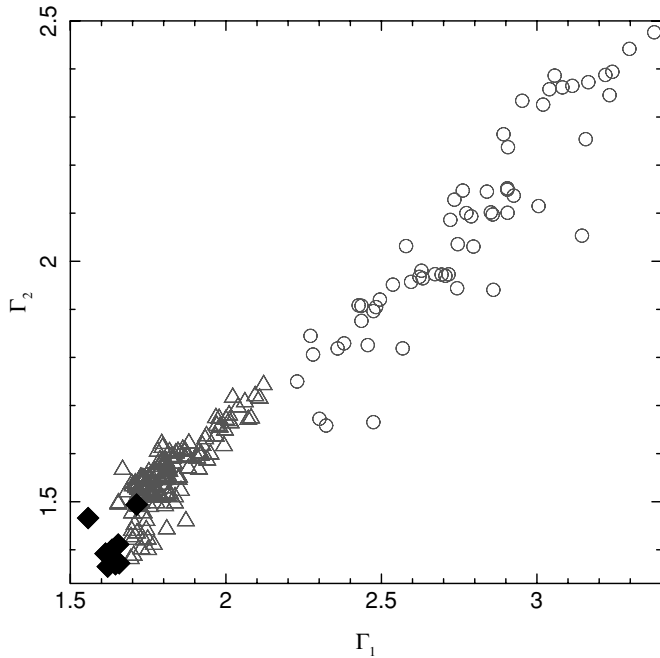


Figure 3. Correlation of the soft X-ray (Γ_1) and hard X-ray (Γ_2) photon indices from exponentially cutoff, broken power-law fits to the *RXTE* Cyg X-1 data presented by Wilms et al. (2006). Triangles represent the hard states ($\Gamma_1 < 2.2$) and circles represent soft states ($\Gamma_2 \geq 2.2$). The solid diamonds represent exponentially cutoff, broken power-law fits to the *RXTE* data discussed in this work. There are spectra from four observations that have been further subdivided into times covering different portions of the color-color diagrams of Figure 2, for a total of nine *RXTE* spectra.

Table 2
Observational Fluxes in keV Energy Bands

Date (yyyy-mm-dd)	0.5–2	2–10 (10^{-8} erg cm $^{-2}$ s $^{-1}$)	10–100	100–300	L_{Bol}^a (L_{Edd})
2006-10-30	0.16	0.78	2.76	1.59	0.032
2007-04-30	0.07	0.55	2.07	1.32	0.026
2007-05-17	0.07	0.38	1.33	0.87	0.017
2008-04-19	0.14	0.72	2.62	1.44	0.035

Notes. Fluxes are absorbed values, are normalized to the PCA spectral fit, and correspond to the brightest/least absorbed periods of the light curves.

^a Unabsorbed, isotropic luminosity in 0.01–800 keV band, expressed as a fraction of Eddington luminosity, as determined from the thermal Comptonization fits of Section 5.1 and assuming a distance of 2.3 kpc and a black hole mass of $10 M_{\odot}$.

does not measure the spectral regime most strongly affected by the dips.

We show the resulting photon indices of these spectra along side the results from Wilms et al. (2006) in Figure 3. Our prior study covered seven years and 202 *RXTE* spectra. These newer observations overlap the historically hardest states measured in that campaign. Specifically, for these new observations Γ_1 ranged from 1.63 to 1.71, which is to be compared to the $\Gamma_1 = 1.65$ minimum found in Wilms et al. (2006). In some cases, these observations also correspond to historically faint hard states of Cyg X-1. Defining the “hard state” as $\Gamma_1 \leq 2.2$, the lowest 2–100 keV flux in the hard state reported by Wilms et al. (2006) was 2.46×10^{-8} erg cm $^{-2}$ s $^{-1}$, while the highest 2–100 keV hard state flux reported in that work was 4.50×10^{-8} erg cm $^{-2}$ s $^{-1}$. As shown in Table 2, the 2–100 keV fluxes spanned by the bright phase, least absorbed observations range from 1.71×10^{-8} to 3.54×10^{-8} erg cm $^{-2}$ s $^{-1}$.

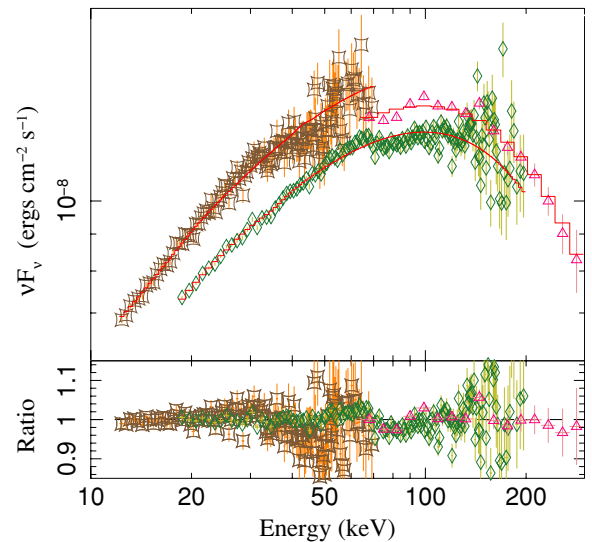


Figure 4. *Suzaku*-HXD PIN (brown squares) and GSO (magenta triangles) spectra, and *RXTE*-HEXTE (green diamonds) spectra from the least absorbed periods of observation 4 fit with an exponentially cutoff power law.

(A color version of this figure is available in the online journal.)

That these spectra are among the faintest and hardest ever observed for Cyg X-1 is important to note. In some models of the black hole hard state, the hardest spectra are expected to have the smallest observed reflection fraction and the disk inner radius should be at a maximum (Zdziarski et al. 1999). However, it is also important to note that other black hole systems can show substantially fainter spectra relative to Eddington luminosity. Furthermore, as we see here and as has been noted elsewhere, the range of hard state fluxes observed in Cyg X-1 spans only a factor of two, and it is unlikely that the bolometric flux spans a much greater factor than this even when including observations from the soft state (Wilms et al. 2006).

As a further comparison to the previously observed hard states, we consider the value of the fitted folding energy. For the hard states discussed by Wilms et al. (2006), the folding energy ranges from ≈ 125 to 255 keV. Other BHCs, e.g., GX 339–4, have shown a wider range of hard state folding energies, i.e., ≈ 50 –300 keV (Wilms et al. 1999; Nowak et al. 2002, 2005; Motta et al. 2009). In our prior studies, we did not consider spectra above 125 keV. Here, however, with the inclusion of the *Suzaku*-GSO spectra we can now consider energy ranges up to 300 keV. For all four of our observations, an exponential rollover is clearly detected. An example is given in Figure 4, which also gives a general indication of the consistency of the cross-correlation among the hard X-ray detectors. The values of the folding energies, along with cross-normalization constants, are given in Table 3. The folding energies range from 164 to 252 keV, nearly the full span encompassed by our prior hard state observations. This is not necessarily surprising. Whereas Wilms et al. (2006) had observed a general trend for the cutoff to increase to higher energies with harder spectra, there was a large degree of scatter about this trend, consistent with these four observations.

4.2. Ionized Absorption Models

Previous *Chandra*-HETG observations of Cyg X-1 have revealed evidence of the ionized, focused wind from the donor star (Miller et al. 2005; Hanke et al. 2009). The effects of this wind upon the spectrum must be accounted for in any

Table 3
constant*highcut*powerlaw Parameters for Hard X-ray Spectra Fits

Date (yyyy-mm-dd)	Γ	A_{PL}	E_{cut} (keV)	E_{fold} (keV)	C_{GSO}	C_{HEXTEA}	C_{HEXTEB}	$B_{\text{HEXTEA}}^{\text{norm}}$	$B_{\text{HEXTEB}}^{\text{norm}}$	χ^2/dof
2006-10-30	$1.41^{+0.02}_{-0.01}$	$1.07^{+0.05}_{-0.03}$	$19.6^{+3.0}_{-2.7}$	183^{+9}_{-5}	$1.007^{+0.008}_{-0.008}$	$0.877^{+0.004}_{-0.004}$	$0.883^{+0.005}_{-0.004}$	$1.12^{+0.01}_{-0.02}$	$1.02^{+0.02}_{-0.01}$	785.4/449
2007-04-30	$1.42^{+0.01}_{-0.01}$	$0.73^{+0.02}_{-0.03}$	$24.6^{+1.8}_{-1.7}$	218^{+7}_{-7}	$0.95^{+0.01}_{-0.01}$	$1.07^{+0.02}_{-0.03}$	$1.07^{+0.02}_{-0.01}$	$1.03^{+0.10}_{-0.06}$	$0.99^{+0.06}_{-0.06}$	966.2/315
2007-05-17	$1.47^{+0.02}_{-0.02}$	$0.60^{+0.04}_{-0.03}$	$23.5^{+3.3}_{-2.7}$	252^{+21}_{-18}	$0.95^{+0.02}_{-0.02}$	301.6/123
2008-04-19	$1.39^{+0.01}_{-0.01}$	$0.93^{+0.02}_{-0.03}$	$20.4^{+1.2}_{-1.3}$	164^{+6}_{-5}	$0.91^{+0.01}_{-0.01}$	$0.837^{+0.003}_{-0.003}$	$0.842^{+0.004}_{-0.004}$	$1.065^{+0.008}_{-0.008}$	$0.99^{+0.01}_{-0.01}$	648.8/447

Notes. Spectra are normalized to HXD-PIN data. E_{cut} , E_{fold} are the cutoff and folding energy of the *highcut* model. A_{pl} is the power-law normalization in photons $\text{keV}^{-1} \text{cm}^{-2} \text{s}^{-1}$ at 1 keV. C are the fit constants for the detectors other than the HXD-PIN. The normalizations of the HEXTE backgrounds were also allowed to be free parameters and are given by the B^{norm} values.

detailed analysis of Cyg X-1. While ionized line absorption is very pronounced during the deepest part of the absorption dips (Figure 1), we stress that such absorption is also significant during the bright phase (non-dip) spectra discussed in this work.

We begin by considering the joint 0.8–7.5 keV *Suzaku* and *Chandra*-HETG spectra from the 2008 April 19 observations. As the MEG spectra are more heavily affected by photon pileup, we fitted only the HEG spectra. We used the same absorbed disk plus power-law (TBnew*(diskbb+powerlaw)) continuum model to fit both the *Suzaku* and HETG spectra. We also added to both spectral models a broad Fe K α line (modeled with diskline; Fabian et al. 1989) and a narrow Fe K α line modeled with a Gaussian, and a 6.7 keV (Fe xxv) absorption line. Following Hanke et al. (2009), we describe the line absorption as a series of Gaussian absorption lines representing a variety of ionized species—predominantly H- and He-like lines from elements ranging from O to Fe, and L-shell transitions of Fe. This initial line list contained nearly 100 line transitions parameterized by wavelength (which we constrained to fall within 1500 km s^{-1} of their rest wavelengths), full-width half-maximum (constrained to be between 5 and 40 mÅ), and line equivalent width. Based upon fits to the joint *Suzaku*-HETG spectra, this initial list was reduced to the 55 significant lines present in the spectra.

The above joint model received two modifications for solely the HETG spectra. The *simple_gp1e2* model (see Hanke et al. 2009) was applied to describe the effects of pileup in the gratings spectra. Owing to this spectrum being fainter and harder than the Cyg X-1 spectrum described in Hanke et al. (2009), these spectra required an even smaller pileup correction. Additionally, we applied the dust scattering model (dustscat) to the HETG spectrum. As described in Section 3, dust scattering represents a loss term for the high spatial resolution *Chandra* spectra. This component, albeit with a time delay of thousands to tens of thousands seconds, scatters back into the *Suzaku* spectrum from arcsecond to arcminute angular scales. To the extent that one can ignore the time evolution of the spectrum, the dust scattering term can be ignored in the *Suzaku* spectra. Lacking any detailed information of the average spectrum prior to the start of our observations, we do not apply any dust scattering correction to the *Suzaku* spectra.

To be explicit, we apply to the *Suzaku* data a model of the form

$$\text{TBnew} * \text{lines} * (\text{diskbb} + \text{powerlaw} + \text{diskline} + \text{gaussian}) \quad (3)$$

while we apply to the HETG data a model of the form

$$\text{simple_gp1e2} \otimes (\text{TBnew} * \text{lines} * \text{dustscat} * (\text{diskbb} + \text{powerlaw} + \text{diskline} + \text{gaussian})), \quad (4)$$

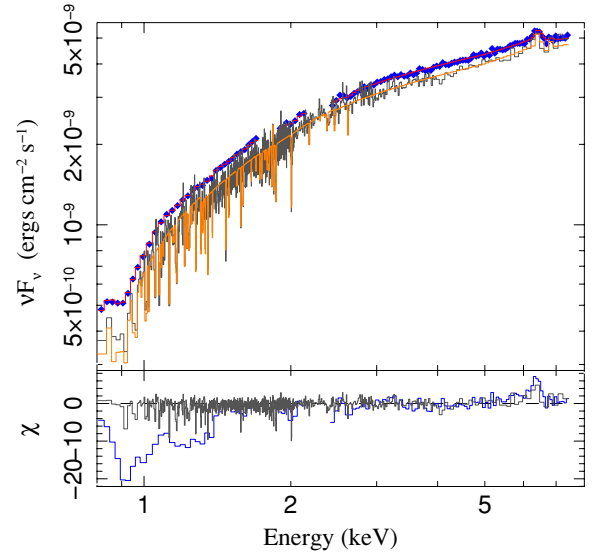


Figure 5. *Suzaku* (blue diamonds) and *Chandra*-HETG (gray histogram; \pm first-order HEG only) data from observation 4. The model consists of absorbed disk and power-law components, broad and narrow Gaussian lines in the Fe K α region, and absorption lines from a variety of highly ionized species, including from Fe xxv at ≈ 6.7 keV. Additionally, we modify the HETG spectra by dust scattering and a pileup term (see the text). The *Suzaku* and HETG spectra have not been renormalized with respect to one another. The residuals shown here are for this joint model fit with all broad and narrow line normalizations (both emission and absorption) set to zero.

(A color version of this figure is available in the online journal.)

where lines represents the ionized line absorption. Throughout the rest of this work, we shall ignore as we are doing here the effects of dust scattering on the *RXTE* and *Suzaku* data. Again, this implicitly assumes that the bright phase spectrum has been steady over the time span of thousands to tens of thousands of seconds. This assumption is unlikely to be valid in detail; however, we lack the data to employ any more sophisticated assumptions.

This simple model describes the spectra well with a dust halo optical depth of 0.25 ± 0.03 (90% confidence level), i.e., consistent with the fits to the color-color diagrams presented in Section 3. This spectral fit is shown in Figure 5. The important point to note here is that the ionized absorption is *extremely* statistically significant in the *Suzaku* spectra, even though the individual lines are not resolved. Inclusion of these lines is vital for obtaining a description of the soft end of the spectrum, and thus we include ionized absorption in all of our model fits. Being that we do not have HETG spectra simultaneous with our other three *Suzaku* spectra, we use the ionized absorption fit presented in Figure 5. Specifically, for all subsequent spectral fits described

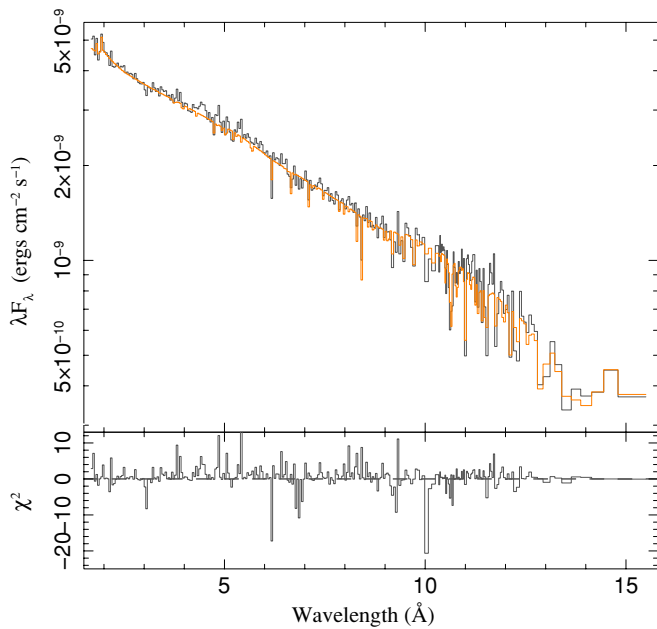


Figure 6. HEG data from a joint fit of the *Suzaku* and *Chandra* data with a simple continuum model (disk, power law, broad and narrow Fe region lines, neutral ISM absorption) plus two ionized absorber components described with the *warmabs* model. The residuals include all of these models components; the remaining line residuals are features not described by the *warmabs* components. (A color version of this figure is available in the online journal.)

in this work, we freeze the line positions, widths, and relative equivalent widths to the values found for this joint fit. The line equivalent widths are tied together via a single normalization constant, and this normalization constant becomes the sole fit parameter describing the ionized absorption. The model, however, still consists of 55 individual absorption lines. As described below, this approach works well in all of our spectral fits.

We explored whether a more sophisticated ionization model could be applied to our data. Rather than fit individual lines to the joint *Suzaku* and *Chandra* data, we instead used the *warmabs* model (Kallman & Bautista 2001) to describe the ionized absorption. A model that includes two ionized components—one with a column of $(7 \pm 4) \times 10^{21} \text{ cm}^{-2}$ and ionization parameter $\log_{10} \xi = 2.77 \pm 0.05$ and the other with a column of $(3 \pm 2) \times 10^{21} \text{ cm}^{-2}$ and ionization parameter $\log_{10} \xi = 1.93 \pm 0.07$ (90% confidence levels), and both with densities of 10^{10} cm^{-3} —describes the data reasonably well. As shown in Figure 6, however, a number of prominent line features are not well fit in the *Chandra* data. Furthermore, aside from being an extremely computationally expensive model to run, when fit to the *Suzaku* data alone the *warmabs* models would tend to gravitate toward low ionization parameter values that, although capable of mimicking some of the continuum features of the *Suzaku* data, did not include the high ionization line features that were clearly present in the *Chandra* data. For these reasons, we choose the empirical approach outlined above.

Several things need to be borne in mind when considering our results: whereas we allow for an overall normalization change in our ionized absorber model, we do not allow for changes of the ionization state. As Figure 5 shows, with the exception of a weak Fe xxv line, there are essentially no ionized lines with energies $\gtrsim 3 \text{ keV}$. Thus, it is unlikely that this simple empirical approach will *directly* impact, for example, broad Fe line studies.

However, in as much as ionization changes could affect our soft X-ray continuum fits, and these continuum fits in turn affect our estimate of the breadth and strength of the red wing of any broad line tail (see Section 5.3), potential ionization changes in this absorber must be considered an additional source of systematic uncertainty in the results discussed below.

4.3. Composite Relativistic Line

The fit described above consisted of both broad and narrow features in the Fe $K\alpha$ region. Here, we examine this spectral region in a somewhat phenomenological manner to gauge the interplay between these narrow and broad features. We wish to consider the average line profile from roughly similar Cyg X-1 spectra. The three most recent *Suzaku* observations occurred closest to orbital phase 0 and show very similar color-color diagrams. As discussed below, these three spectra are fit with comparable ionized absorption normalization constants. We therefore consider these spectra jointly and ignore the first *Suzaku* observation. We fit these spectra with a model consisting of a power law, narrow emission near 6.4 keV and narrow absorption near 6.7 keV, plus a relativistically broadened Fe line (again using the *diskline* model). The relativistically broadened line is characterized by a broad tail extending redward from the line rest-frame energy and a sharper peak (due to Doppler boosting) blueward of the line rest-frame energy.

For purposes of this discussion, we allow the power law to assume independent parameter values for each of the *Suzaku* observations. The energies and widths of the narrow lines are tied together for all three observations, but the line strengths are fitted individually. The broad line has an energy fixed to 6.4 keV and an emissivity index fixed to $\beta = -3$ (i.e., line emissivity is $\propto R^{-3}$, where R is the emission radius within the disk), and the disk inclination is fixed at 35° (the value adopted by Herrero et al. 1995 from the middle of the range of suggested inclinations). The inner radius of the broad line emission is tied together for all three observations, but the line strengths are left independent. The χ^2 of the fit is determined from the sum of χ^2 values from the individual observations; however, in Figure 7 we show the spectra, fitted models, and residuals from the combined data. We fit the spectra only in the 4.5–7.5 keV bandpass.

These joint fits strongly require the presence of a broad line. The broad line is significantly detected in each individual XIS detector from each individual observation. Under the assumptions of the continuum model applied here, the broad line equivalent width is approximately three times that of the narrow line equivalent width. The best fit inner radius for the broad line emission is $10.6^{+2.9}_{-1.6} GM/c^2$ (90% confidence level), i.e., close to the ISCO for a Schwarzschild black hole. As we will discuss further in Section 5.1, the specific value for such an inner radius is dependent upon the fitted continuum. Nevertheless, a broad excess is required redward of the Fe $K\alpha$ line.

In describing the residuals in this region with a broad line, we see that the Fe xxv absorption line occurs near the blue wing peak of the relativistically broadened line (Figure 7). Both the narrow emission and absorption lines in the Fe region are required in the HETG spectra when considered by themselves (see also Hanke et al. 2009), and thus they cannot be ignored in the *Suzaku* spectra. The HETG spectra, however, are not particularly well suited for describing any broad component of the Fe line. (See Figure 8 and the discussion of Hanke et al. 2009 concerning broad line fits to our prior joint *RXTE-Chandra*-HETG observations of Cyg X-1.)

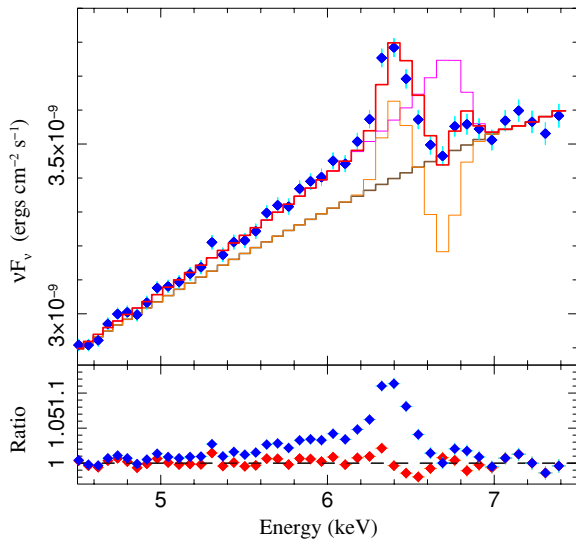


Figure 7. Summed unfolded *Suzaku* spectra from unabsorbed periods from observations 2–4, as shown in the Fe $K\alpha$ line region. These data have been fit with a model consisting of an absorbed power law, narrow Fe $K\alpha$ emission line, narrow Fe xxv absorption line, and a relativistically broadened diskline model. (See the text for fitting procedures.) The individual model components (power law, with added disk line, and separately with added narrow emission and absorption lines) are shown overlain on the spectra, while the residuals are shown with and without the emission and absorption line components.

(A color version of this figure is available in the online journal.)

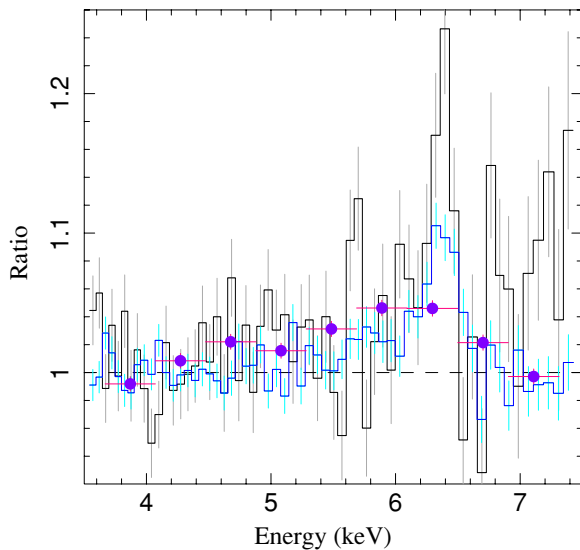


Figure 8. *Suzaku* (blue line), *Chandra*-HEG (gray line), and *RXTE*-PCA (purple diamonds) residuals from fitting an absorbed power law to the 3.5–4.5 keV and 7–7.5 keV regions simultaneously. The *Chandra*-HEG data have been binned to match approximately the binning of the *Suzaku* data.

(A color version of this figure is available in the online journal.)

On the other hand, if we compare the *RXTE* spectra to both the *Suzaku* and HETG spectra, we find that the *RXTE* spectra alone require an Fe line equivalent width that cannot be accommodated with solely the narrow line component from the *Suzaku*-HETG fit. We highlight this fact in Figure 8, where we show the residuals from a power-law fit in the 3.5–4.5 keV and 7–7.5 keV region to the joint *RXTE*-*Suzaku*-HETG spectra. In this figure, we have binned the HETG spectra to match approximately the binning of the *Suzaku* spectra. There is overall good agreement between the *RXTE* and *Suzaku* residuals; both require a broad red wing in the Fe line region. The narrow Fe $K\alpha$ emission and Fe xxv absorption are clearly seen in the HETG spectra;

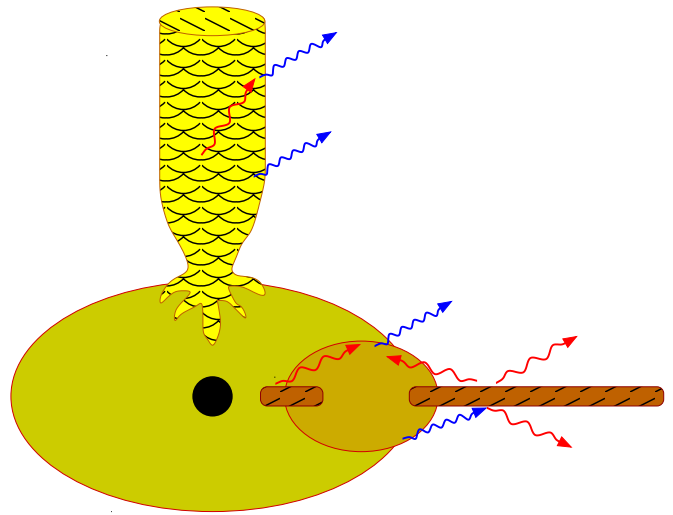


Figure 9. Possible X-ray emission geometry of the Cyg X-1 system. Part of the soft X-rays likely come from an accretion disk, which may be truncated at its inner edge by a hot corona. Two possible (of many suggested) geometries are shown for this corona: a torus and a quasi-spherical cloud. In some models, the disk can reform in the inner regions of the accretion flow (Mayer & Pringle 2007). The corona will Compton upscatter a fraction of the disk component(s) soft X-rays to hard X-rays. Whether or not the corona envelopes the disk(s) determines whether or not an additional, un-Comptonized disk component should be present in the spectra. (If the disk reforms on the inner edge of a toroidal corona, for example, a fraction of its soft X-rays will not intersect the corona.) Hard X-rays will be reprocessed into reflection/fluorescent line components, predominantly by the outer disk. Finally, the jet might contribute to the observed X-ray emission via synchrotron and synchrotron self-Compton emission.

(A color version of this figure is available in the online journal.)

however, when viewed by itself, any broad Fe line component in the HETG spectra could be subsumed via a slight power-law slope change. We ascribe this latter fact to remaining calibration issues in the HETG detector. Based upon these results, we include broad and narrow Fe $K\alpha$ emission and narrow Fe xxv absorption in all the subsequent fits presented in this work. As we shall discuss below, however, the implied broad line parameters are dependent upon the assumed continuum model.

5. BROADBAND MODELS

We now turn to a discussion of the 0.8–300 keV, joint *Suzaku*–*RXTE* spectra for the bright phases of our four Cyg X-1 observations. Here, we consider three different Comptonization models, two of which are discussed in detail, and a jet model. (“Toy geometries” for some of these situations are presented in Figure 9.) The latter model also contains Comptonization components that represent both Comptonization of disk photons as well as SSC. The non-jet models discussed below all rely upon the *eqpair* model (Coppi 1999, 2005) to describe the fitted Comptonization components.

5.1. Comptonization Descriptions

The *eqpair* model allows for Comptonization by a coronal electron population that has both thermal and non-thermal energy distributions. The latter distribution is governed by a parameterized power law, which for purposes of the fits described here we left at the default *eqpair* values. Specifically, the electron phase space density follows a distribution $\propto E^{-2}$, where E is the electron energy, between energies of 1.3 eV and 1 MeV. The *eqpair* model rather than being parameterized by a coronal electron scattering optical depth and temperature is instead parameterized by a *seed* electron optical depth (pair production

within the corona, accounted for in the code, can yield higher net scattering optical depths) and coronal compactness parameters, ℓ (proportional to component luminosity or power divided by radius). The latter parameters are divided into two relative compactness parameters: ℓ_h/ℓ_s the coronal compactness divided by the seed photon compactness, and ℓ_{nt}/ℓ_h the compactness of the non-thermal electron population divided by the total electron population compactness. Over a wide range of parameters, the hardness of the spectrum and the temperature of the corona increases with increasing compactness (although pair production can modify that effect).

The seed photon spectrum can be set to either a blackbody or a disk spectrum (essentially the `diskp` model from XSPEC; Gierliński et al. 1999). We choose the latter seed photon spectrum, with the peak temperature of this disk (kT_{disk1}) becoming a fit parameter. We also allow for an unscattered disk component by including an additional `diskbb` component with peak temperature fixed to the peak temperature of the seed photons. Our choice for the normalization of this component depends upon the specific Comptonization model under consideration (see below).

To account for soft excesses (i.e., below ≈ 1.5 keV) in the spectra, we sometimes include an additional unscattered disk component with freely varying normalization and temperature (A_{disk2} , kT_{disk2}). We searched for, and easily found, solutions where the peak temperature of this unscattered disk component was below ≈ 300 eV. The `eqpair` model includes reflection from an ionized disk (i.e., a modification of the `pexriv` model; Done et al. 1992), which is smeared by relativistic distortions with the emissivity profile of a Shakura–Sunyaev type disk (Shakura & Sunyaev 1973). A fittable parameter is the inner radius of this disk smearing profile (see below). We also fix the disk (i.e., reflector) temperature to 10^6 K, the reflector inclination to 35° , and allow the reflection fraction ($\Omega/2\pi$) and reflector ionization parameter (ξ) to be fit parameters. The latter is limited to values ≤ 1000 .

Line absorption is described by the parameterized (i.e., single normalization constant) model discussed in Section 4.2. A narrow Gaussian is added at 6.399 keV with its width frozen to 0.01 keV, but with a freely variable normalization. A `diskline` component (essentially the profile for a disk around a Schwarzschild black hole; Fabian et al. 1989) is added to describe the broad line. Its energy is fixed to 6.4 keV, the disk line emissivity index is set to $\beta = -3$, and the disk inclination is set to 35° . Typically one allows the inner emission radius to be variable (see Section 4.3). Here, we tie this inner radius to that of the reflector in the `eqpair` model. The line normalization, however, is allowed to freely vary.

A number of authors have considered “sphere+disk” Comptonization models wherein an inner quasi-spherical corona is encircled by a cool, geometrically thin disk that typically has a peak temperature of ≈ 200 eV (Gierliński et al. 1997; Dove et al. 1997b). We were unable to find any solutions for coronae with thermal electron distributions (i.e., ℓ_{nt}/ℓ_h frozen at 10^{-3}) that allowed for such a low seed photon temperature. The only such thermal corona solutions that we found required seed photon temperatures of 0.8–1 keV. Fit parameters for these solutions are presented in Table 4, and spectral fits are shown in Figure 10.

Concepts for the potential geometry represented by this spectral fit are shown in Figure 9. The high temperature seed photons could be a recondensed inner disk as envisioned by Mayer & Pringle (2007), while the low temperature soft excess, the broad line, and the reflection component could

emanate from an outer disk. (The narrow line likely arises from fluorescence from the secondary and/or spatially extended gas surrounding the system; Torrejón et al. 2010.) A more physically self-consistent model would allow for an additional seed photon contribution from this outer disk, and possibly a broad line component from the inner, hot seed photon emission region. However, it is interesting to note that these solutions required very little additional unscattered, high temperature disk component. (Table 4 contains low—sometimes zero—values of A_{disk1} . Both the initial seed photon distribution and the associated high temperature, unscattered disk spectrum are shown in Figure 10; the former is much more significant.) The amplitude of the soft seed photon contribution and the weakness of an additional unscattered high temperature disk would indicate a “recondensed” disk region of only modest extent, predominantly within the confines of a more extended corona, from which we would expect little iron line contribution.

On the other hand, these spectral fits do require an additional, unscattered low temperature disk component. The values of A_{disk2} presented in Table 4 correspond to inner disk radii of ≈ 2 – 10 GM/c^2 , given a distance of 2.3 kpc, a black hole mass of $10 M_\odot$, and an inclination of 35° . This is roughly consistent with the inner radius of the fitted broad Fe line and relativistically smeared reflector, for which we find values ranging from $R_{\text{in}} = 6$ – 18 GM/c^2 . (The inner emission radius of the line appears to be uncorrelated with the inner radius implied by the normalization of the low temperature disk component.) These radii values are roughly consistent with values close to the marginally stable orbit of a Schwarzschild black hole.

The broad line amplitude is between 6 and 22 times the amplitude of the narrow line component. Fitted reflection fractions are $\Omega/2\pi \approx 0.2$.

Comparable high seed photon temperature fits were found by Wilms et al. (2006) when considering solely *RXTE* spectra. The major difference between those fits and the ones discussed here is that our prior fits also required a significant contribution from an unscattered, high temperature disk. It is unclear whether that difference is due to the inclusion of *Suzaku* data that extend to lower energies, the inclusion here of ionized absorption, or the fact that these spectra are for the most part fainter and harder than those discussed by Wilms et al. (2006). The coronal compactnesses found here are comparable to the maximum values from our previous studies, while the seed optical depths are slightly lower (by ≈ 0.3 – 0.5 for comparable observations). These values of seed optical depth and compactness correspond to coronal temperatures of 85–115 keV and total optical depths of 1.1–1.4. The fitted reflection fractions are slightly higher here (by ≈ 0.05) than those fits with comparable ℓ_h/ℓ_s from Wilms et al. (2006).

We have found a set of Comptonization model solutions that do allow for a low seed photon temperature. For these fits, we include only one extra unscattered disk component (with its peak temperature tied to the peak seed photon temperature), and we further tie the inner disk radius to the inner radii of the `eqpair` reflector and the `diskline` emissivity. That is, we are explicitly mimicking the “sphere+disk” geometry (albeit not in a completely self-consistent manner) shown in Figure 9. If we then relax the assumption of a purely thermal coronal electron distribution, good descriptions of the spectra are found with low seed photon temperatures. The ratio of non-thermal to total coronal compactness then falls in the range $\ell_{nt}/\ell_h = 0.01$ – 0.82 . That is, up to 82% of the electron energy (presuming that the thermal and non-thermal electrons are cospatial) resides in a

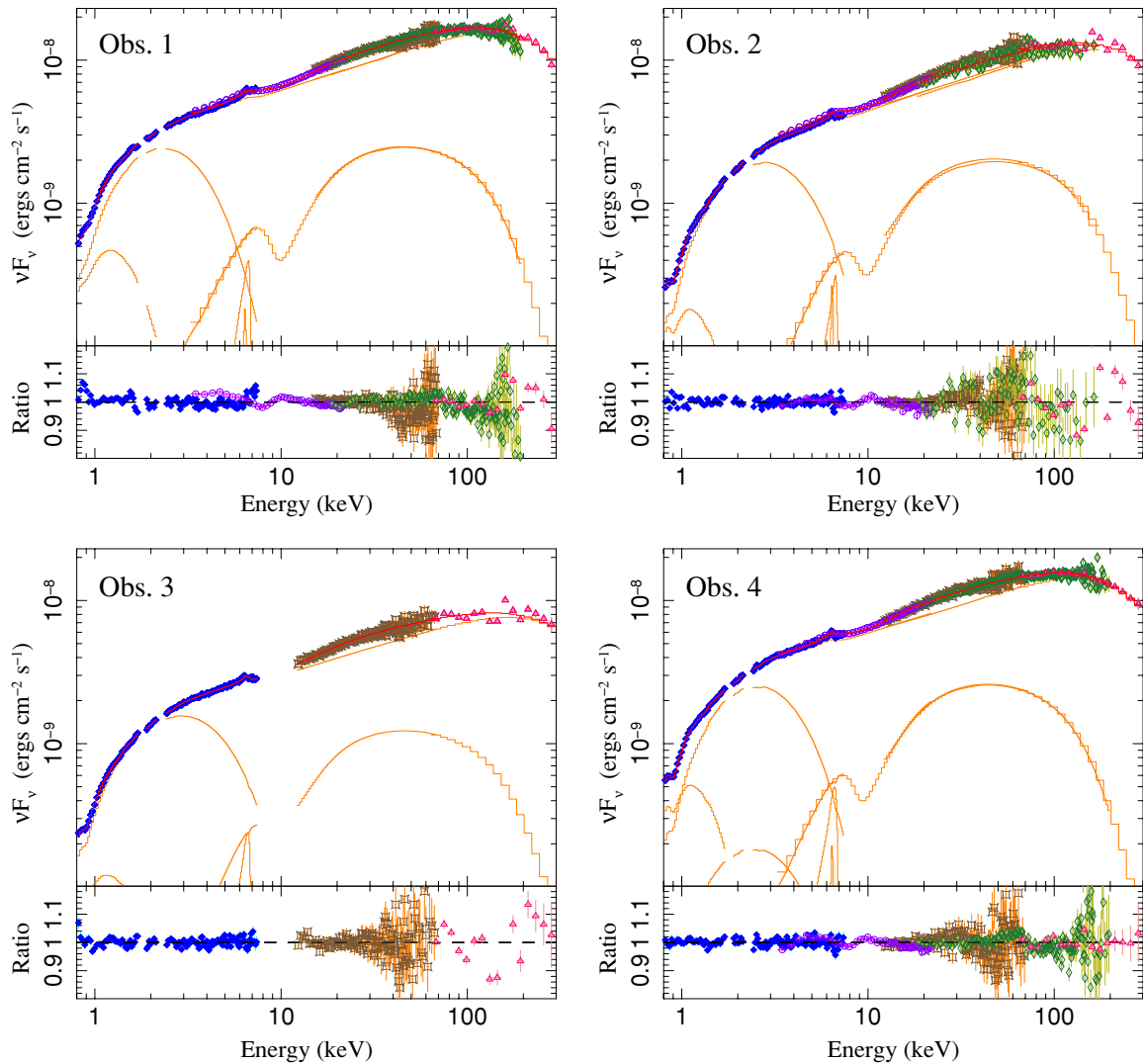


Figure 10. Unfolded *Suzaku* and *RXTE* spectra, plus model components and fit residuals from the high kT_{seed} , thermal corona *eqpair* fits. *Suzaku*-XIS spectra from individual detectors/data modes and *RXTE*-HEXTE spectra from each cluster were summed for the figures, but not for the fits. Here, and throughout the remainder of this paper, XIS data are filled blue diamonds, PCA data are hollow purple circles, PIN data are hollow green diamonds, HEXTE data are brown squares, and GSO data are hollow magenta triangles. The following model components are shown: the summed model with the reflection component excluded, the reflection component by itself, the broad and narrow Fe $K\alpha$ line components, the seed photons without Comptonization applied, the additional disk component with peak temperature tied to the seed photons, and the additional low temperature disk component. Neutral and ionized absorption are applied to all shown model components.

power-law distribution that extends to 1 MeV. Parameters for this model are presented in Table 5 and spectra are shown in Figure 11.

The quality of these fits is similar to or perhaps slightly better than that for the thermal corona fits. The fitted compactness parameters for the non-thermal coronae are approximately double those for the thermal fits. (Similar results were found by Ibragimov et al. 2005 when comparing thermal and non-thermal *eqpair* fits.) At first glance, the optical depths seem smaller; however, owing to the large coronal compactnesses pair production is significant and the net optical depths range from 0.7 to 1.6, while the thermal electrons have temperatures that range from 55 to 160 keV. Reflection fractions are slightly larger (by up to 0.09) for these fits. The broad line inner radius in some cases has increased, and now ranges from $\approx 6\text{--}32 GM/c^2$. Additionally, the amplitude of the broad line is now only 3–13 times that of the narrow line. This difference compared to the thermal corona model is due to two factors: the narrow line amplitude is slightly increased, while the broad line amplitude in two cases is nearly halved.

We briefly consider one other thermal Comptonization solution that allows for a low seed photon temperature. (No “toy geometry” for this model is shown in Figure 9.) It is a model similar to that considered by Frontera et al. (2001) when modeling *BeppoSAX* spectra of Cyg X-1 and to that considered by Makishima et al. (2008) when modeling *Suzaku* spectra of Cyg X-1. In these models two *eqpair* components are included. They share the same seed photon temperature (tied to the peak temperature of an additional unscattered disk component, as before), and they share the same reflection parameters; however, they have independent compactness and optical depths. An example of such a model fit is shown in Figure 12. These fits are generally successful, but no so more than the previous two models. Furthermore, owing to the larger degree of freedom given the two semi-independent coronal components, they are fraught with local minima representing qualitatively different relative contributions of the two Comptonization components. We do not consider these more complex models further in this work, other than to point out that such double corona solutions as discussed by Makishima et al. (2008) and Frontera et al. (2001) can

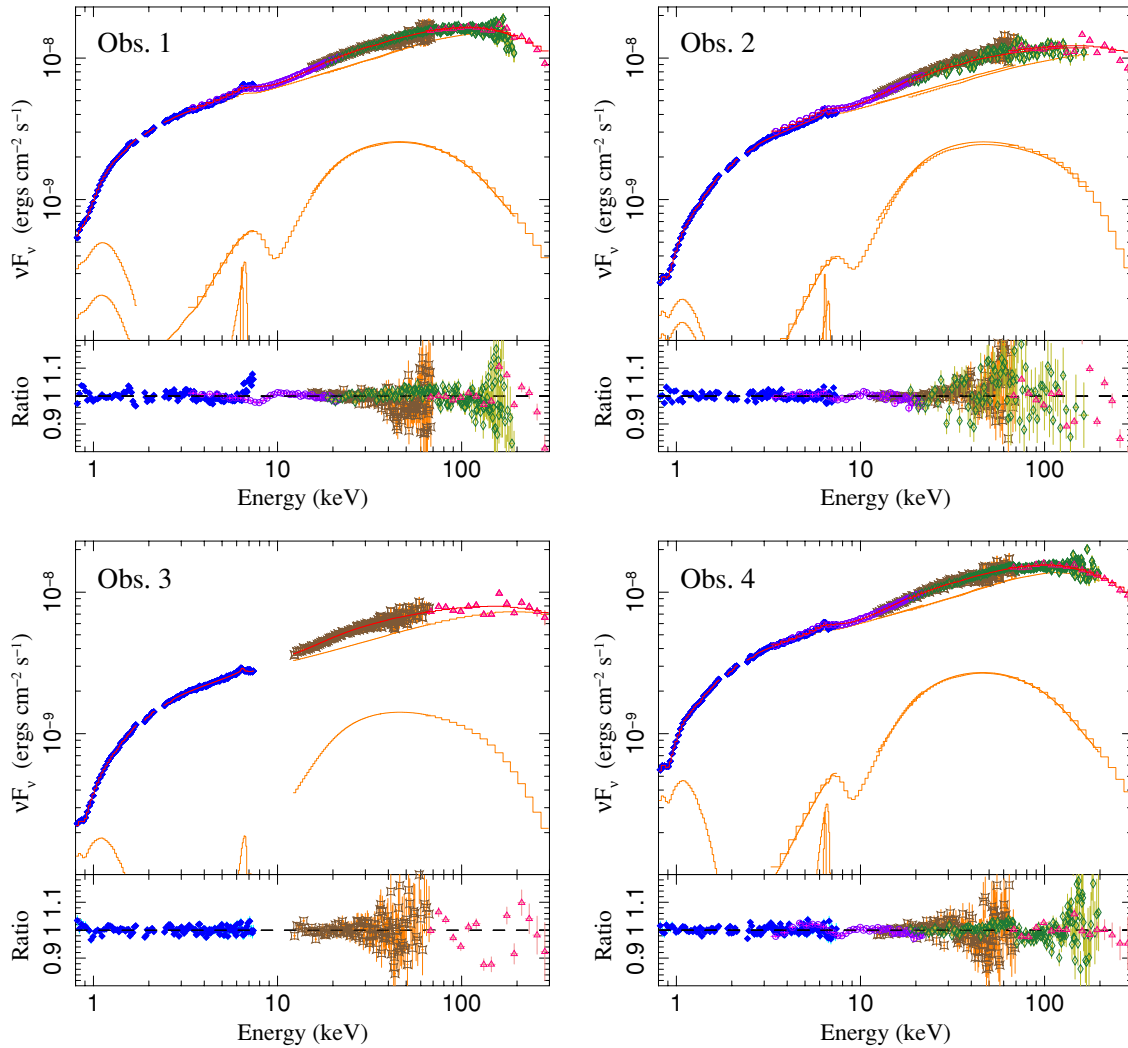


Figure 11. Same as Figure 10, but for the non-thermal corona, low kT_{seed} `eqpair` model fits. The following model components are shown: the summed model with the reflection component excluded, the reflection component by itself, the broad and narrow Fe $K\alpha$ line components, the seed photons without Comptonization applied, and the additional disk component with peak temperature tied to the seed photon peak temperature. Neutral and ionized absorption are applied to all shown model components.

allow for both low seed photon temperature and purely thermal coronae.

5.2. Jet Descriptions

The Compton corona models described above provide a good description of the 0.8–300 keV spectra. These models, however, are not unique. Even within the restricted class of coronal models, we have shown three qualitatively different solutions that yield comparable fits. Furthermore, none of the Compton corona models give a self-consistent description of the correlated radio spectra. Although the four observations discussed here did not have simultaneous radio spectra, our prior studies (Gleissner et al. 2004b; Nowak et al. 2005; Wilms et al. 2006) allow us to make good estimates of what the correlated 15 GHz radio flux likely was. We describe this estimated joint radio/X-ray spectrum with the jet model of Markoff et al. (2005) and Maitra et al. (2009).

It is important to distinguish the jet models as discussed in Markoff & Nowak (2004), Markoff et al. (2005), and later works from the earlier iteration of the jet model discussed in Markoff et al. (2001, 2003). The 2001/2003 work considered a parameter space where only synchrotron radiation from the jet

contributed to the observed X-rays. Later work, and the version of the jet model used here, include X-rays produced not only by jet synchrotron radiation, but also by jet SSC processes and Comptonization of seed photons from the disk. The synchrotron component is only mildly beamed, with peak $\beta \sim 2$ in the radio emitting portions of the jet. The inverse Comptonization component comes from near the jet base where $\beta \sim 0.4$, and thus undergoes very little beaming. Thus, although this does mean that the fitted jet parameters are dependent upon assumed inclination angle (e.g., the jet input power, N_j will depend upon assumed inclination), given the low β values inherent in the model it is possible to find good fit parameters for a wide variety of assumed inclinations.

A full description of the main jet model parameters can be found in the Appendix of Markoff et al. (2005) and in Maitra et al. (2009). The version of the jet model that we use is closest to that discussed in Maitra et al. (2009); therefore, we repeat part of the model parameter summary presented there. We assume a distance of 2.5 kpc and an inclination of 35° for the Cyg X-1 system. The jet properties are then determined by the input jet power (N_j , expressed as a fraction of the Eddington luminosity for a $10 M_\odot$ black hole), the electron temperature of

Table 4
Parameters for Thermal Comptonization Spectral Fits

Date (yyyy-mm-dd)	N_{H} (10^{22} cm^{-2})	A_{eqp} (10^{-3})	$\ell_{\text{h}}/\ell_{\text{s}}$	τ_p	$\Omega/2\pi$	ξ ($4\pi F_{\text{ion}}/n$)	R_{in} (GM/c^2)	A_{disk1}	kT_{disk1} (keV)	A_{disk2} (10^4)	kT_{disk2} (keV)	A_{diskline} (10^{-3})	A_{line} (10^{-4})	C_{lines}	χ^2/dof
2006-10-30	$0.72^{+0.01}_{-0.01}$	$5.007^{+0.001}_{-0.001}$	$7.47^{+0.01}_{-0.01}$	$1.446^{+0.005}_{-0.005}$	$0.194^{+0.002}_{-0.001}$	1000_{-33}	$17.4^{+0.1}_{-0.1}$	$14.5^{+0.7}_{-1.4}$	$0.848^{+0.001}_{-0.001}$	$4.18^{+0.02}_{-0.04}$	$0.258^{+0.001}_{-0.001}$	$6.3^{+0.7}_{-0.3}$	$8.2^{+3.1}_{-1.8}$	$0.39^{+0.03}_{-0.02}$	2469/975
2007-04-30	$0.82^{+0.01}_{-0.01}$	$3.586^{+0.003}_{-0.004}$	$7.55^{+0.02}_{-0.02}$	$1.228^{+0.005}_{-0.005}$	$0.219^{+0.003}_{-0.002}$	1000_{-79}	$8.9^{+0.1}_{-0.1}$	$0.0^{+0.3}$	$0.986^{+0.001}_{-0.001}$	$13.8^{+0.2}_{-0.1}$	$0.191^{+0.001}_{-0.001}$	$5.0^{+0.4}_{-0.4}$	$8.7^{+1.5}_{-1.6}$	$0.93^{+0.02}_{-0.03}$	2035/842
2007-05-17	$0.63^{+0.04}_{-0.02}$	$1.573^{+0.001}_{-0.021}$	$6.61^{+0.31}_{-0.25}$	$0.976^{+0.029}_{-0.025}$	$0.210^{+0.028}_{-0.025}$	1000_{-83}	$6.0^{+0.5}$	$0.0^{+0.7}$	$1.130^{+0.051}_{-0.098}$	$1.18^{+0.02}_{-0.45}$	$0.250^{+0.018}_{-0.031}$	$4.4^{+0.6}_{-0.7}$	$2.0^{+2.0}_{-1.8}$	$0.53^{+0.08}_{-0.08}$	851/483
2008-04-19	$0.82^{+0.04}_{-0.03}$	$7.816^{+0.007}_{-0.102}$	$6.95^{+0.08}_{-0.08}$	$1.431^{+0.002}_{-0.009}$	$0.238^{+0.011}_{-0.009}$	732^{+132}_{-122}	$6.0^{+0.3}$	$39.5^{+2.6}_{-8.0}$	$0.852^{+0.035}_{-0.001}$	$29.2^{+11.3}_{-7.3}$	$0.197^{+0.001}_{-0.002}$	$9.2^{+1.0}_{-1.4}$	$6.5^{+3.5}_{-4.1}$	$1.07^{+0.01}_{-0.02}$	1610/843

Notes. See the text for a description of the model. Spectra are normalized to PCA data. Disk normalizations are $(R_{\text{in}}/D)^2 \cos \theta$, where R_{in} is the inner disk radius in units of km, D is the source distance in units of 10 kpc, and θ is the inclination. Line normalizations are integrated photon flux in the lines ($\gamma/\text{cm}^2 \text{ s}^{-1}$). Error bars are 90% confidence level for one interesting parameter.

Table 5
Parameters for Non-thermal Comptonization Spectral Fits

Date (yyyy-mm-dd)	N_{H} (10^{22} cm^{-2})	A_{eqp}	$\ell_{\text{h}}/\ell_{\text{s}}$	$\ell_{\text{nt}}/\ell_{\text{h}}$	τ_p	$\Omega/2\pi$	ξ ($4\pi F_{\text{ion}}/n$)	R_{in} (GM/c^2)	kT_{disk1} (keV)	A_{diskline} (10^{-3})	A_{line} (10^{-4})	C_{lines}	χ^2/DoF
2006-10-30	$0.81^{+0.01}_{-0.01}$	$2.229^{+0.027}_{-0.082}$	$16.04^{+0.01}_{-0.13}$	$0.82^{+0.01}_{-0.01}$	$1.39^{+0.03}_{-0.02}$	$0.211^{+0.001}_{-0.008}$	499^{+31}_{-56}	$6.7^{+0.1}_{-0.1}$	$0.192^{+0.002}_{-0.001}$	$6.6^{+0.9}_{-0.9}$	$11.1^{+3.1}_{-2.9}$	$0.32^{+0.06}_{-0.06}$	2254/977
2007-04-30	$0.96^{+0.01}_{-0.01}$	$3.158^{+0.003}_{-0.005}$	$13.29^{+0.33}_{-0.23}$	$0.01^{+0.01}_{-0.01}$	$0.40^{+0.01}_{-0.06}$	$0.305^{+0.010}_{-0.001}$	97^{+10}_{-2}	$13.3^{+0.1}_{-0.1}$	$0.158^{+0.001}_{-0.001}$	$3.0^{+0.6}_{-0.6}$	$9.7^{+1.9}_{-1.9}$	$0.85^{+0.02}_{-0.02}$	1919/844
2007-05-17	$0.86^{+0.10}_{-0.02}$	$1.811^{+0.383}_{-0.072}$	$12.98^{+0.82}_{-0.98}$	$0.36^{+0.01}_{-0.03}$	$0.01^{+0.43}_{-0.01}$	$0.257^{+0.038}_{-0.026}$	0^{+18}	$6.3^{+2.0}_{-0.3}$	$0.175^{+0.003}_{-0.002}$	$3.4^{+0.6}_{-0.7}$	$2.6^{+1.8}_{-1.9}$	$0.81^{+0.07}_{-0.09}$	810/485
2008-04-19	$1.08^{+0.02}_{-0.01}$	$1.338^{+0.011}_{-0.113}$	$15.28^{+0.16}_{-0.02}$	$0.78^{+0.14}_{-0.02}$	$1.41^{+0.01}_{-0.02}$	$0.239^{+0.017}_{-0.002}$	189^{+43}_{-66}	$32.3^{+1.8}_{-0.2}$	$0.150^{+0.001}_{-0.001}$	$4.1^{+1.0}_{-1.0}$	$9.4^{+3.5}_{-4.4}$	$1.00^{+0.07}_{-0.07}$	1535/845

Notes. See the text for a description of the model. Spectra are normalized to PCA data. Disk normalizations are $(R_{\text{in}}/D)^2 \cos \theta$, where R_{in} is the inner disk radius in units of km, D is the source distance in units of 10 kpc, and θ is the inclination. Line normalizations are integrated photon flux in the lines ($\gamma/\text{cm}^2 \text{ s}^{-1}$). Error bars are 90% confidence level for one interesting parameter.

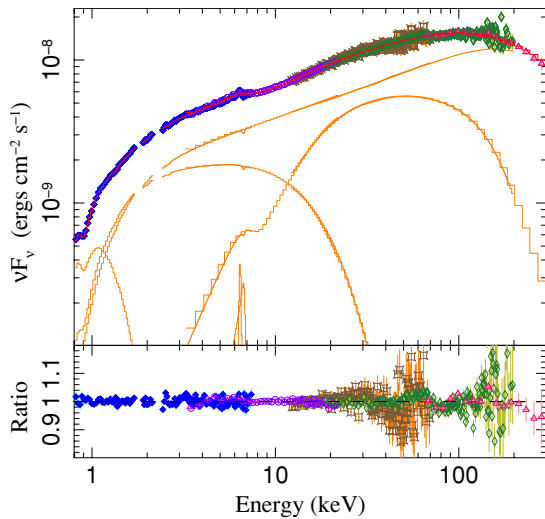


Figure 12. Same as Figure 10, but only showing observation 4 for the multiple `eqpair` component fit (see the text). The following model components are shown: the two individual `eqpair` components with their reflection components excluded, the reflection component of the dominant `eqpair` spectrum, the broad and narrow $\text{Fe K}\alpha$ line components, and the unscattered disk component.

the relativistic thermal plasma entering at the jet base (T_e), the ratio of magnetic to particle energy density (the equipartition factor, k), the physical dimensions of the jet base (assumed to be cylindrical with radius R_0 and height h_0 , the latter fixed to $1.5 R_0$), and the location of the point on the jet (z_{acc}) beyond which a significant fraction of the leptons are accelerated to a power-law energy distribution that follows E^{-p} , with p being a fit parameter. The fit parameter ϵ_{acc} can be physically interpreted as being related to the particle acceleration rate (which is $\propto \epsilon_{\text{acc}}^{-1}$; see Markoff et al. 2001).

As for the corona-only models, we also include emission from a low temperature disk with inner radius R_{in} and peak temperature T_{disk1} . (This disk is very similar in temperature and normalization to the low temperature disk component included in the Comptonization model fits.) A relativistically broadened $\text{Fe K}\alpha$ line (with the same emissivity and inclination parameters as for the corona-only models) is coupled to the disk component by having its inner radius of emission tied to the disk inner radius. A narrow Gaussian line is included, as well as a reflection component (calculated with the `reflect` model from XSPEC). Unlike the reflection model internal to the `eqpair` code, the `reflect` model, which performs a convolution on any given input spectrum, does not account for relativistic smearing. The Fe edge near 7.1 keV in this unsmeared reflected spectrum can produce a sharp feature not seen in the data residuals; therefore, we smear this component with a unit-normalized, $\sigma = 1$ keV Gaussian convolution.¹³

Fit results for this model are presented in Table 6 and Figures 13 and 14. The overall quality of these fits is quite good, although not quite as good as for the corona-only models discussed above. The jet models leave slightly larger residuals in the PCA spectra (near the Fe line region and the 10 keV region),

¹³ Kernels for relativistic smearing do exist, e.g., the models of Brenneman & Reynolds (2006). The jet model calculations, however, are already substantially slower than the Compton corona calculations. Coupling them with the computationally expensive relativistic kernel would make the fits discussed here prohibitively time consuming to run. Furthermore, the jet model reflection geometry is likely more complex than that of the standard Compton corona: it should have separate contributions for the synchrotron, SSC, and Comptonized disk photons (see Markoff & Nowak 2004). For these reasons we chose a very simple smearing profile.

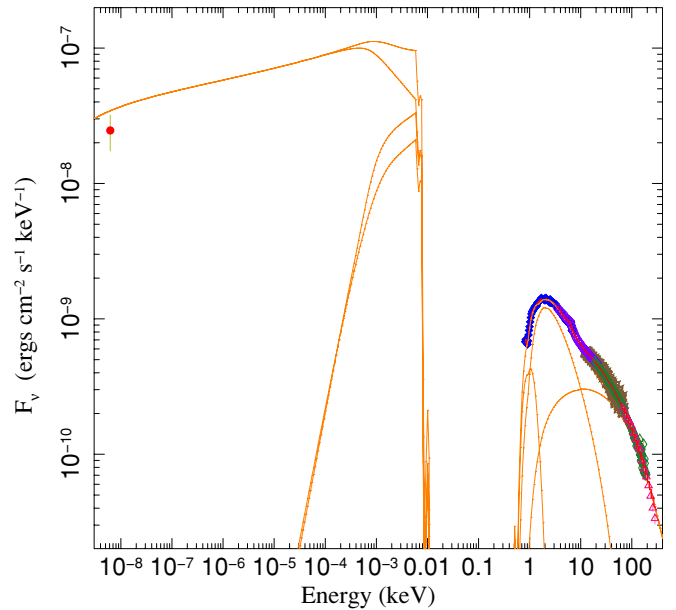


Figure 13. Jet model fit to the estimated radio flux and measured X-ray spectra from observation 4. Individual model components are shown with both neutral and ionized absorption applied. We show the summed model, as well as the jet synchrotron component, the jet SSC component, the Compton corona component, and the disk component.

as well as in the GSO spectra. The former could be related to inadequate modeling of the reflection spectrum (i.e., not using a relativistically smeared model).

Fits to the hardest X-ray spectra (i.e., the cutoff seen in the GSO) are governed by the jet SSC and the inverse Compton components. This latter component is comprised of a magnetized, beamed corona with a high temperature ($\approx (3-5) \times 10^{10}$ K, i.e., $\approx 3-5$ MeV), and low electron scattering optical depth ($\tau_{\text{es}} \lesssim 0.01$). A high temperature, low optical depth corona with a limited residence time under those conditions simplifies the jet code by allowing one to use a single scattering approximation for calculating the Comptonization spectrum. The compactness of such a corona, however, could lead to high pair production which would then serve to cool the corona and increase its optical depth (see, for example, the critique of Malzac et al. 2009).

Post-facto estimates of the physical self-consistency of fitted jet models are discussed by Maitra et al. (2009) who calculate the pair production and annihilation rates at the base of the corona. Fits to the hard state spectra of XTE J1181+105 yield far higher annihilation rates than production rates, and therefore represent a self-consistent solution. Fits to the hard state spectra of GX 339-4 yield mixed results. For some cases, annihilation and production rates are comparable and the resulting corona is marginally self-consistent. In other cases, the calculated production rates are an order of magnitude higher than annihilation rates, and the resulting coronae are not self-consistent (Maitra et al. 2009).

We have performed the same calculations as discussed by Maitra et al. (2009) for jet models fitted in this work and find that all yield pair production rates larger than pair annihilation rates. The coronae within these jet models are therefore not self-consistent. Observation 3 produces a fit that is closest to being self-consistent, with pair production and annihilation rates being a factor ≈ 10 apart from one another. Jet fits to the other observations are further from self-consistency.

Such inconsistencies were similarly true for early coronal models, e.g., those based upon the work of Haardt & Maraschi

Table 6
Parameters for Jet-dominated Spectral Fits

Date (yyyy-mm-dd)	N_{H} (10^{22} cm^{-2})	N_{j} ($10^{-2} L_{\mathrm{Edd}}$)	R_0 (GM/c^2)	z_{acc} (GM/c^2)	ϵ_{acc} (10^{-4})	p	k	T_{e} (10^{10} K)	R_{in} (GM/c^2)	T_{disk1} (10^6 K)	$\Omega/2\pi$	A_{diskline} (10^{-3})	A_{line} (10^{-4})	C_{lines}	χ^2/dof
2006-10-30	$0.86^{+0.01}_{-0.01}$	$3.07^{+0.01}_{-0.07}$	$2.28^{+0.01}_{-0.01}$	$66.9^{+11.9}_{-0.1}$	$0.89^{+0.01}_{-0.01}$	$2.08^{+0.01}_{-0.01}$	$1.75^{+0.30}_{-0.15}$	$3.27^{+0.03}_{-0.01}$	$7.1^{+0.1}_{-0.5}$	$2.34^{+0.03}_{-0.01}$	$0.11^{+0.01}_{-0.01}$	$11.2^{+0.7}_{-0.8}$	$8.1^{+2.0}_{-2.8}$	$0.38^{+0.06}_{-0.03}$	2444/976
2007-04-30	$1.15^{+0.01}_{-0.02}$	$3.22^{+0.05}_{-0.01}$	$2.27^{+0.01}_{-0.01}$	$126.1^{+0.1}_{-6.8}$	$1.43^{+0.01}_{-0.01}$	$1.79^{+0.01}_{-0.01}$	$0.10^{+0.01}_{-0.01}$	$5.15^{+0.01}_{-0.01}$	$28.4^{+0.8}_{-1.1}$	$1.66^{+0.02}_{-0.01}$	$0.30^{+0.02}_{-0.01}$	$3.9^{+0.5}_{-0.4}$	$7.7^{+2.0}_{-2.0}$	$0.84^{+0.06}_{-0.06}$	2042/843
2007-05-17	$0.96^{+0.01}_{-0.01}$	$1.02^{+0.01}_{-0.05}$	$77.2^{+2.0}_{-4.2}$	$59.0^{+1.8}_{-0.2}$	$1.62^{+0.03}_{-0.02}$	$2.33^{+0.01}_{-0.01}$	$4.54^{+0.16}_{-0.09}$	$4.14^{+0.02}_{-0.02}$	$15.5^{+0.2}_{-0.3}$	$1.72^{+0.01}_{-0.01}$	$0.34^{+0.03}_{-0.01}$	$1.5^{+0.3}_{-0.5}$	$3.4^{+1.7}_{-1.5}$	$0.46^{+0.06}_{-0.02}$	831/484
2008-04-19	$1.00^{+0.01}_{-0.01}$	$3.83^{+0.01}_{-0.02}$	$2.00^{+0.10}_{-0.02}$	428^{+110}_{-1}	$0.73^{+0.01}_{-0.01}$	$1.70^{+0.01}_{-0.01}$	$0.39^{+0.01}_{-0.01}$	$3.75^{+0.05}_{-0.06}$	$22.9^{+0.4}_{-0.6}$	$1.86^{+0.01}_{-0.01}$	$0.24^{+0.01}_{-0.01}$	$6.9^{+0.8}_{-0.9}$	$8.9^{+4.1}_{-4.1}$	$1.01^{+0.07}_{-0.06}$	1543/844

Notes. See the text for a description of the model. Spectra are normalized to PCA data. Line normalizations are integrated photon flux in the lines ($\gamma/\mathrm{cm}^2 \text{ s}^{-1}$). Error bars are 90% confidence level for one interesting parameter.

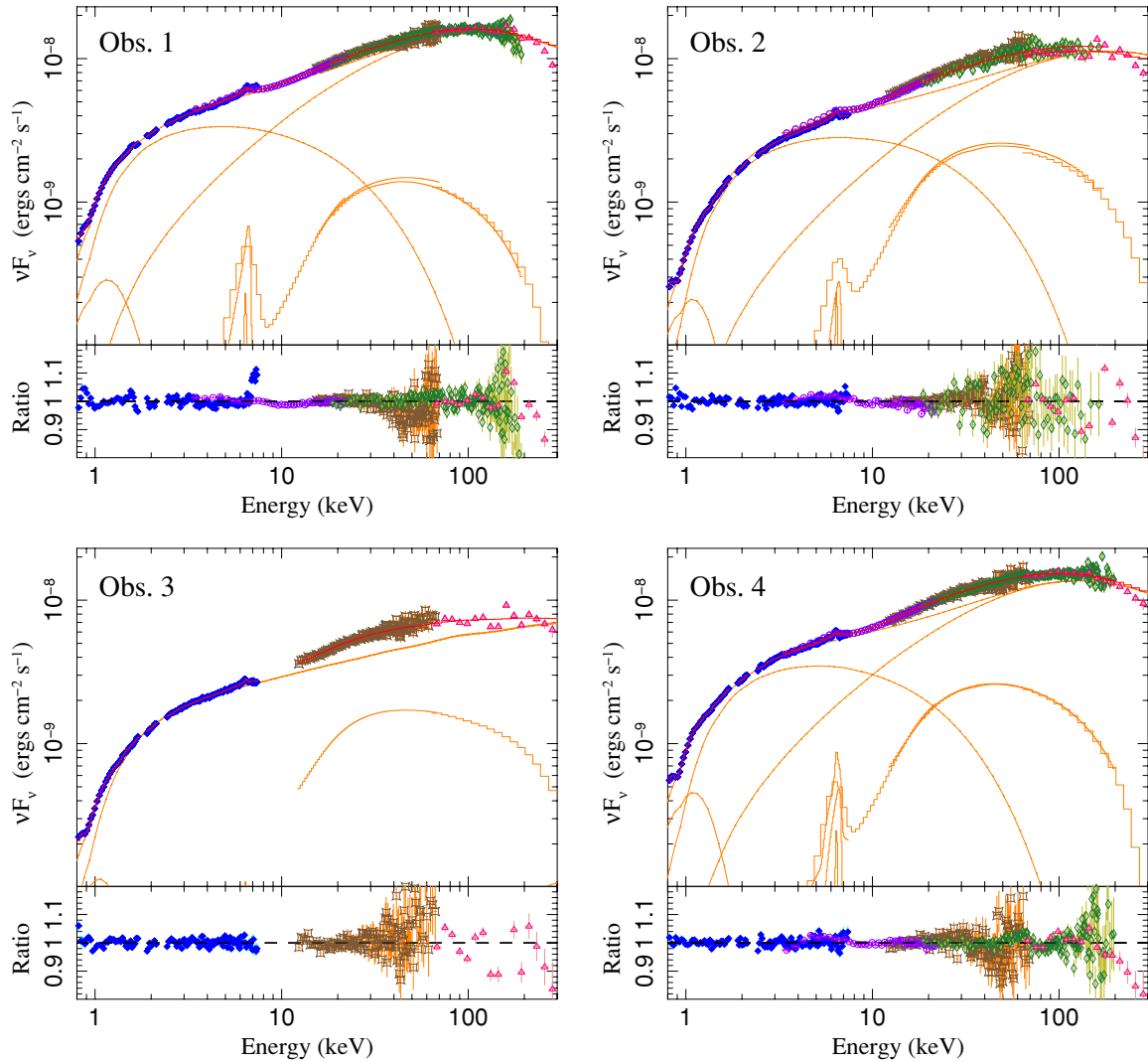


Figure 14. Same as Figure 10, but for the jet model fits. The following model components are shown: the summed model with the reflection component excluded, the reflection component by itself, the broad and narrow Fe $K\alpha$ line components, the jet synchrotron component (which dominates the 2–10 keV spectra for observations 1, 2, and 4), the jet SSC component (which dominates the 100–300 keV spectra for observations 1, 2, and 4), and the disk component. Neutral and ionized absorption are applied to all shown model components.

(1991). A number of such “slab geometry” coroneae, in order to produce the hardest X-ray spectra observed in sources such as Cyg X-1, used coronal temperatures (apart from any consideration of pair production) that were unachievable in those geometries (see the discussion of this issue by Dove et al. 1997a). Such inconsistencies were in fact what led to the development of more physically self-consistent coronal models, e.g., the *kotelp* model of Stern et al. (1995) and Dove et al. (1997b) and the *eqpair* model of Coppi (1999).

We consider these jet models, however, as they are as of yet the only spectral models that make a serious attempt to explain the correlated radio spectra. Future iterations of these models will incorporate consideration of pair production, as well as synchrotron and SSC cooling of the Compton corona (A. Pe’er & S. Markoff 2011, in preparation). (As shown by Dove et al. 1997a and others, coronal cooling can be a more significant consideration than pair production in some situations.)

The derived parameters are similar to those found for fits to other BHCs (see the fits to XTE J1118+105 and GX 339–4 presented by Maitra et al. 2009). The power input at the base of the jet, in terms of Eddington luminosity, is comparable to the inferred bolometric luminosity (i.e., compare the values

of N_j to the values of Table 2; although different inclination assumptions will alter the value of N_j , given the low β values in the jet, it is always comparable to the inferred system luminosity). The radius of the base of the jet is comparable to the radius of the ISCO. The largest fit value exceeds the ISCO for a Schwarzschild black hole by only a factor of 11. The shock acceleration distance along the jet, z_{acc} ranges from ≈ 60 – $430 GM/c^2$. The former value is comparable to that found for XTE J1118+105, while the latter is comparable to that found for GX 339–4. As discussed above, the fitted coronal electron temperatures at the base of the jet range from $\approx (3\text{--}5) \times 10^{10}$ K. Work in progress suggests that a physically self-consistent coronal temperature that properly accounts for the dominant effects of synchrotron and SSC cooling may truncate the allowed range of coronal temperatures to the lower end found here (A. Pe’er & S. Markoff 2011, in preparation). Future versions of the jet code will explicitly account for these effects.

For all the fits presented in Figure 14, both synchrotron and SSC radiation make substantial contributions to observed X-ray spectra. This is an important point to which we shall return in Section 6.

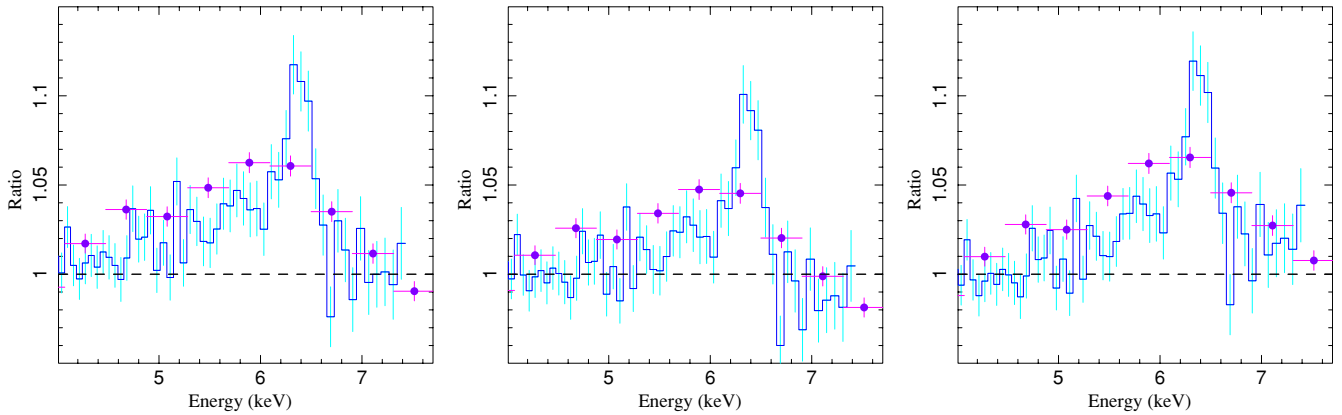


Figure 15. Fe $K\alpha$ line region residuals for observation 4, obtained from our best fits by setting the broad and narrow line normalizations (including the normalization of the Fe xxv absorption line) to zero. Left: the high kT_{seed} *eqpair* fit, the hybrid thermal/non-thermal *eqpair* fit, and the jet model fit. (Purple circles are the *RXTE* residuals, while the blue histograms are the *Suzaku* residuals.)

(A color version of this figure is available in the online journal.)

5.3. Comparison of Implied Relativistic Lines

In Figure 15, we show the Fe line region residuals for the two Compton corona models and the jet model. These residuals are derived by setting the line normalizations (including absorption line normalizations) to zero, *without* refitting. They are also different from line residuals that are often used for illustrative purposes where only a portion of the continuum outside of the line region is fit with a simple power law (e.g., Figure 7). The residuals in Figure 15 are meant to highlight the differences in the derived line parameters for the three main continuum models discussed here.

As shown by the parameters in Tables 4–6, there are indeed differences among the inferred line parameters. For the most part, the purely thermal Comptonization model yields the strongest line equivalent widths, while the non-thermal Comptonization model yields the weakest equivalent widths (by up to a factor of two). The thermal Comptonization model usually also yields the smallest inner radii for the relativistically broadened line, in some cases extending all the way to the ISCO for a Schwarzschild black hole. Larger values of these radii, however, are typically found with the other two models. These differences are evident in the lower energy residuals shown in Figure 7.

To be clear, a substantially broadened line is *required* by *all* spectral models that we have explored, and there is a good agreement between the PCA and *Suzaku*-XIS residuals regarding this fact. We also reiterate that for all explored models, the equivalent width of the fitted narrow line (typically <15 eV) is only a fraction of that for the broad line, and is in fact substantially smaller than the Fe line equivalent width we have found for any model that we have applied to any *RXTE* observation of Cyg X-1 (Wilms et al. 2006). Furthermore, for these four observations, we have not found any implied inner radius greater than $\approx 40 GM/c^2$. The precise details of this broadened line, however, do depend upon the assumed continuum model.

6. DISCUSSION

In this work, we present broadband (0.8–300 keV) fits to four separate observations of Cyg X-1 that have simultaneous *Suzaku* and *RXTE* data. The most recent of these observations also has simultaneous *Chandra*-HETG data. Each of these observations shows evidence of dipping events likely due to dense structures (“clumps”) in the otherwise highly ionized wind

of the secondary. This is seen in the light curves (Figure 1), and the color–color diagrams (Figure 2, which can be modeled by the presence of a dust scattering halo). The ionized absorption is very significant in the *Suzaku* spectra (Figure 5) even though in this work we consider the least absorbed periods of the light curve. *Modeling the ionized line absorption present in Cyg X-1, via the use of parameterized fits to the HETG spectra, is crucial for deriving good fits to the soft X-ray spectra seen by Suzaku and RXTE.*

We note that even accounting for this ionized absorption, the spectral fits presented in this paper yield reduced χ^2_v that range from 1.8 to 2.5. Do such values truly represent good fits to these data? Cyg X-1 is bright, and these observations are of sufficient length that the signal-to-noise values for these spectra are quite high. The spectra are dominated by systematic errors, especially at the soft X-ray energies. We already have added 0.5% systematic errors to the PCA spectra, which is a reasonable estimate for the *internal* uncertainty of the PCA. There are also relative uncertainties among the detectors. For observation 4, if we increase the PCA systematic errors to 1%, add 1% systematic errors to the HEXTE A cluster (i.e., the fixed cluster), and add 3% systematic errors to the *Suzaku*-XIS spectra, then the fits presented here would have reduced $\chi^2_v \approx 1$. Comparing the fits among the individual XIS spectra (representing both different individual detectors and different data acquisition modes), we have found that $\pm 3\%$ is a reasonable estimate of the end-to-end differences among these spectra. We hypothesize that the quality of the fits presented here is near “optimal” given the current internal and relative calibrations of these detectors.

The observations that occurred on 2007 May 17, i.e., the third set of observations, are potentially the most problematic in terms of cross-calibration issues. For our other sets of observations, the *RXTE*-PCA data act as a “bridge” between the *Suzaku*-XIS and -PIN spectra. Each can have its relative normalization anchored by a comparison to the PCA, which overlaps the energy coverage of both detectors. This is lacking in the third observation, leading to the worry that changes in the normalization constant are subsuming, for example, continuum spectra associated with the spectral break at ≈ 10 keV. For the third observation, we find the ratio of the PIN to XIS 1 normalization constant to range from 1.10 to 1.17. This is to be compared to the 1.16–1.18 value found for fits to the first observation, the 1.06–1.08 found for the second observation, and the 1.10–1.11 found for the

fourth observation. The expected value¹⁴ for the PIN/XIS 0 comparison is 1.16. There is some amount of scatter for the cross-normalization values among the different observations; however, the first, second, and fourth observations show little scatter in its value for different fits to the same data. More scatter is seen for the third observation; therefore, additional systematic uncertainties need to be considered as being present for that set of observations.

Using simple broken power law and exponentially cutoff power-law fits, we find that these spectra are among the hardest seen in the “low hard state” of Cyg X-1 over the past decade. For all four observations, the spectra are clearly detected out to 300 keV with the GSO, and exponential cutoffs are well constrained. *Although these are among the hardest Cyg X-1 spectra ever detected, the exponential folding energies vary by over a factor 1.5, and range from 160 to 250 keV.*

Historically observed hard state spectra in Cyg X-1 have shown folding energies that vary over a slightly wider range, while hard state BHC as a class show folding energies that span a factor of five.

As these spectra are among the faintest and hardest for Cyg X-1, they make excellent test beds for theoretical models that posit, for instance, that the hard state represents a configuration with an inner disk that has evaporated into a quasi-spherical corona. In such a scenario, we might expect these spectra to show the most “extreme” recession of the inner disk, although we have noted that the bolometric luminosities represented by these spectra only span a factor of two. At a few percent of the Eddington luminosity, they are not far below the expected soft-to-hard state transition. Numerous transient BHC sources show much fainter hard states as they fade into quiescence.

We have presented a number of different spectral models, all of which describe the 0.8–300 keV spectra well. Some of these models describe the X-ray spectra primarily with Comptonization components (whether due to a thermal or hybrid thermal/non-thermal corona), while the jet model is dominated by synchrotron and SSC emission from the jet. All of these models have a number of features in common.

1. All models require a soft excess that here we describe with a disk component with low ($kT_{\text{disk}} \approx 200$ eV) peak temperature. The implied inner radii of these disks range from 2 to 40 GM/c^2 .
2. All models require a relativistically broadened line component. The inner emission radius of this broadened line never exceeds $\approx 40 GM/c^2$, but for some models is as low as 6 GM/c^2 .
3. All models require a reflection component. The typical values for the reflection fraction are $\Omega/2\pi \approx 0.2$ –0.3.
4. All models imply that the spectral hardening at ≈ 10 keV is not *solely* due to reflection.

This latter point is very important, and broadly agrees with similar conclusions drawn by Frontera et al. (2001), Ibragimov et al. (2005), and Makishima et al. (2008). The presence of the broad Fe line and *some* of the spectral curvature in the 20–300 keV band is a clear indication of the presence of reflection. However, this reflection spectrum is *not* sitting on top of a simple “disk+powerlaw” spectrum. There is additional continuum complexity separate from reflection that contributes to this perceived break. A high seed photon temperature in the

thermal corona model yields a soft excess in the 2–10 keV band and thus contributes to the measured break in that scenario. (See the discussion in Wilms et al. 2006.) As has been discussed by Ibragimov et al. (2005), a non-thermal electron population in the corona can lead to a soft excess in the 2–10 keV band that helps contribute to what otherwise would be modeled as a reflection break at 10 keV. The two corona model discussed by Makishima et al. (2008), a version of which is shown in Figure 12, rather explicitly replaces part of the reflection component with a broadband continuum model. Finally, in the jet paradigm the spectral break at 10 keV is partly attributable to the transition from dominance by synchrotron emission to SSC emission in the continuum.

There are plausible physical scenarios for each of the discussed spectral models, with some hypothesized geometries being shown in Figure 9. The hybrid thermal/non-thermal coronal model is the closest to the concept of the quasi-spherical inner corona with outer geometrically thin disk (e.g., Eardley et al. 1975; Shapiro et al. 1976; Ichimaru 1977; Dove et al. 1997b, etc.). We have only been able to find such solutions, however, when invoking a partly non-thermal electron population in the corona.

The purely thermal coronal model contains two disk components that are reminiscent of the physical description given by Mayer & Pringle (2007). These authors describe a situation where an outer, geometrically thin, cool disk surrounds an inner, geometrically thick, hot corona. In the very inner radii of this corona, however, thermal conduction leads to it condensing into a geometrically thin and optically thick disk (see Figure 9). Such a component could supply the high temperature seed photons in our thermal corona solutions, while the lower temperature outer disk could provide the bulk of the reflection features. The jet model has a natural physical interpretation in that the usually observed optically thick radio spectrum observed in the hard state is clear indication of the presence of a jet. The question that remains is the contribution of this component to the X-ray band.

The fact that the continuum is more complex than a simple “disk+powerlaw,” yet there are multiple, physically motivated models that yield comparably good spectral fits, leads to the final point: *Although a relativistically broadened line is required in all of our spectral models, the parameters of this line are dependent upon the presumed continuum model.*

Coupled with this dependence upon assumed continuum spectrum is an implicit dependence upon ionized absorption, for which we have detailed *Chandra*-HETG measurements for only the fourth observation.¹⁵ Again, we have not found an inner radius for this line that exceeds $\approx 40 GM/c^2$. Given the variations of this line with presumed continuum, however, we are as of yet unable to use this line for more refined diagnostics such as estimates of black hole spin.

Although we are unable as of yet to draw firm conclusions as to the best geometry and physical mechanisms to describe the hard state spectra of Cyg X-1, these new joint *Suzaku*–*RXTE* data provide a stunning contrast to our prior results using solely *RXTE* data (Wilms et al. 2006). For the *RXTE* data alone we were able to describe the 3–125 keV spectra with a variety of

¹⁴ <http://heasarc.gsfc.nasa.gov/docs/suzaku/analysis/watchout.html>. Since we did not fit XIS 0 data for the fourth observation, here we compare to XIS 1.

¹⁵ Since performing these observations, we have carried out a *Chandra*-HETG observation of orbital phase 0.5 (PI: Nowak), and have an approved observation of orbital phase 0.25 (PI: Hanke). Coupled with archival *Chandra*-HETG observations of orbital phases near 0.75, we hope to develop a better understanding of how the ionized absorption evolves with orbital phase, which should allow us to improve our spectral modeling in the future.

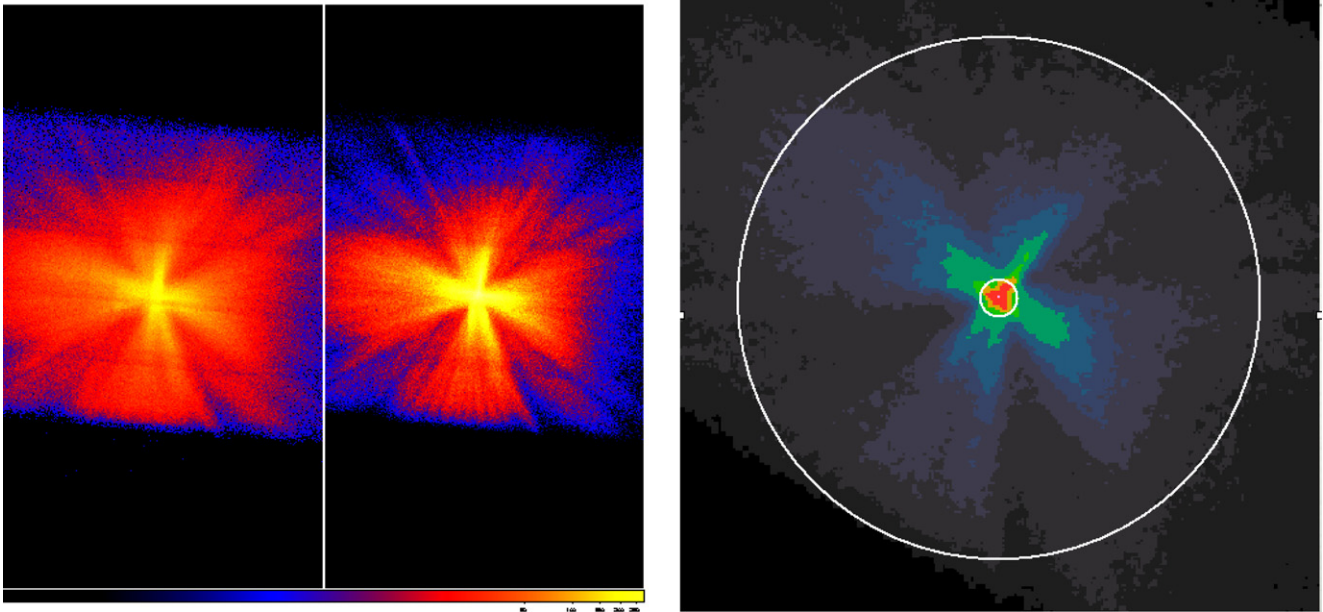


Figure 16. Left: an example of *Suzaku* attitude correction. The left half of the image shows a Cyg X-1 image using the standard attitude correction. The right half of the image shows the improvement with `aeattcorr.sl`. Right: an image of Cyg X-1 where discrete colors correspond to the pileup in that region. The outer white circle denotes the outer boundary of an annular extraction region and the inner white circle denotes the inner boundary. Pileup fractions within this excluded region are as high as 35%. The average effective residual pileup level is $<4\%$.

physically motivated Comptonization models and to describe correlations among the fit parameters. On the other hand, the simple exponentially cutoff, broken power-law models with a single, broad Gaussian line described the data equally well, if not better (Wilms et al. 2006). When considering the 0.8–300 keV *Suzaku*–*RXTE* data discussed here, this is no longer the case. We now require complex absorption at low energy, an asymmetric broad line plus narrow emission and absorption components in the Fe line region, and a complex continuum model. The catalog of *Suzaku* observations of BHC will continue to increase such that we observe a wider variety of BHC states and luminosities. Furthermore the sophistication and physical self-consistency of the spectral models will continue to improve. Together, they offer the promise of obtaining a better understanding of the physical processes occurring in these BHC systems.

We thank the *RXTE*, *Suzaku*, and *Chandra* schedulers for making these simultaneous observations possible. This work was supported by *Suzaku* and *Chandra* guest observer grants, NNX07AF71G, NNX08AE23G, NNX08AZ66G, GO8-9036X, as well as NASA Grant SV3-73016. M.H. and J.W. acknowledge the support of the BMWi through DLR Grant 50 OR 0701. The research in this work has been partially funded by the European Commission under grant ITN 215212. S.M. and D.M. acknowledge support from a Netherlands Organization for Scientific Research (NWO) Vidi and OC Fellowship, respectively.

APPENDIX

SUZAKU ATTITUDE CORRECTION AND PILEUP ESTIMATION

We have created two tools to aid our *Suzaku* data analysis: `aeattcor.sl` and `pile_estimate.sl`. The tools, descriptions of their use, and example results can be found at <http://space.mit.edu/ASC/software/suzaku>. The former tool further corrects the *Suzaku* attitude solution, whereas the latter es-

timates the degree of pileup in a given subset of the observation. Both are scripts written in S-Lang but are designed to be run on a terminal command line using ISIS, the Interactive Spectral Analysis System (Houck & Denicola 2000), as a driver. For all intents and purposes, the scripts behave similar to the typical Unix command line tools found in the HEASOFT package.

Thermal flexing of the *Suzaku* spacecraft leads to a slow wobbling of the optical axis, and hence blurring of the image. Current *Suzaku* tools partially correct this effect by adjusting the spacecraft attitude file based upon details of the spacecraft orbit, temperature, etc. (Uchiyama et al. 2008). `aeattcor.sl` further improves this correction (Figure 16) for a bright source by using its time-dependent detected image to create a new attitude file. Specifically, the tool attempts to shift the time-dependent mean detector image position to a new specified, fixed sky position. It presumes that there are no intrinsic variations in the time-dependent image position. (A mean image position may be time varying, for example, if it is comprised of two or more variable sources of comparable flux. Additionally, a highly variable and piled up source where an “image crater” appears and disappears over the course of the observation may lead to a variable mean image position.) The bin time over which the tool searches for and shifts the image peak is a user selectable parameter; however, we have used the default of 100 s.

We applied the tool to detector images that first underwent the standard attitude correction process (Uchiyama et al. 2008). We chose circular regions with radius $\approx 2'$ that were visually centered on the source image. The tool then created a new attitude correction file, which we applied with the `xiscoord` tool. All of our attitude correction files were created using solely the XIS 1 images.

Pileup occurs in CCD detectors when two or more photons fall on the same or neighboring pixels during the same readout frame, and therefore are read as a single higher energy photon or are discarded as a bad event (Davis 2001). `pile_estimate.sl` was run after `aeattcor.sl`, as uncorrected blurring leads to an underestimate of the degree of pileup.

The tool first creates a light curve in three energy bands, using both rate and counts. Here, we used the default values of 0.5–1.5 keV, 1.5–3 keV, and 3–9 keV for the energy bands and 32 s for the time bins. These data are then passed to the `vwhere` (Noble 2005) filtering tool. The `vwhere` tool was used to create the color–intensity diagrams shown in Figure 2), and it was used to select times of approximately uniform rates and colors (see Section 3). These time selections were then written to a filter file used for subsequent data extraction using the `xselect` tool.

A box-car smoothed (3×3 pixel bins) image is displayed using the `ds9` tool, with the image rescaled to the estimated pileup fraction. Pileup fraction here is defined to be the ratio of events lost via grade or energy migration to the events expected in the absence of pileup. Furthermore, the pileup fraction is based upon the mean counts per 3×3 pixel region per readout frame. The image displays discrete steps that represent the minimum pileup fraction in the displayed region, with the exception of the highest displayed value. This value corresponds to the image maximum, and is shown over regions at this maximum down to half way toward the next lowest displayed value.

Using this image, we chose to exclude the central regions with pileup fractions $\gtrsim 10\%$ (Figure 16). Typically, this was an $\approx 20''$ radius region, comprising $\approx 1/3$ of the detected events. The `pile_estimate.sl` tool then gives an estimate of the mean level of the remaining pileup fraction in the image, which for these data was typically $< 4\%$.

REFERENCES

- Bałucińska-Church, M., Church, M. J., Charles, P. A., Nagase, F., LaSala, J., & Barnard, R. 2000, *MNRAS*, **311**, 861
- Beloborodov, A. M. 1999, *ApJ*, **510**, L123
- Böck, M., Wilms, J., Grinberg, V., Pottschmidt, K., Hanke, M., Markoff, S., Nowak, M. A., & Pirner, S. 2010, in AIP Conf. Ser. 1248, Proc. X-ray Astronomy 2009, ed. A. Comastri, L. Angelini, & M. Cappi (Melville, NY: AIP), 143
- Brenneman, L. W., & Reynolds, C. S. 2006, *ApJ*, **652**, 1028
- Canizares, C. R., et al. 2005, *PASP*, **117**, 1144
- Coppi, P. 1999, in ASP Conf. Ser. 161, High Energy Processes in Accreting Black Holes, ed. J. Poutanen & R. Svensson (San Francisco, CA: ASP), 375
- Coppi, P. 2005, in AIP Conf. Ser. 714, X-ray Timing 2003 Rossi and Beyond, ed. P. Kaaret, F. K. Lamb, & J. H. Swank (Melville, NY: AIP), 79
- Davis, J. E. 2001, *ApJ*, **562**, 575
- Done, C., Mulchaey, J. S., Mushotzky, R. F., & Arnaud, K. A. 1992, *ApJ*, **395**, 275
- Dove, J. B., Wilms, J., & Begelman, M. C. 1997a, *ApJ*, **487**, 747
- Dove, J. B., Wilms, J., Maisack, M. G., & Begelman, M. C. 1997b, *ApJ*, **487**, 759
- Dove, J. B., Wilms, J., Nowak, M. A., Vaughan, B. A., & Begelman, M. C. 1998, *MNRAS*, **298**, 729
- Eardley, D. M., Lightman, A. P., & Shapiro, S. L. 1975, *ApJ*, **199**, L153
- Fabian, A. C., Rees, M. J., Stella, L., & White, N. E. 1989, *MNRAS*, **238**, 729
- Fender, R. P., Stirling, A. M., Spencer, R. E., Brown, I., Pooley, G. G., Muxlow, T. W. B., & Miller-Jones, J. C. A. 2006, *MNRAS*, **369**, 603
- Frontera, F., et al. 2001, *ApJ*, **546**, 1027
- Gierliński, M., Zdziarski, A. A., Done, C., Johnson, W. N., Ebisawa, K., Ueda, Y., Haardt, F., & Philips, B. F. 1997, *MNRAS*, **288**, 958
- Gierliński, M., Zdziarski, A. A., Poutanen, J., Coppi, P. S., Ebisawa, K., & Johnson, W. N. 1999, *MNRAS*, **309**, 496
- Gleissner, T., Wilms, J., Pottschmidt, K., Uttley, P., Nowak, M. A., & Staubert, R. 2004a, *A&A*, **414**, 1091
- Gleissner, T., et al. 2004b, *A&A*, **425**, 1061
- Haardt, F., & Maraschi, L. 1991, *ApJ*, **380**, L51
- Hanke, M., Wilms, J., Boeck, M., Nowak, M., Schulz, N., Pottschmidt, K., & Lee, J. 2008, in VII Microquasar Workshop: Microquasars and Beyond, ed. E. K. et al. (Trieste: Proceedings of Science), 16
- Hanke, M., Wilms, J., Nowak, M. A., Pottschmidt, K., Schulz, N. S., & Lee, J. C. 2009, *ApJ*, **690**, 330
- Herrero, A., Kudritzki, R. P., Gabler, R., Vilchez, J. M., & Gabler, A. 1995, *A&A*, **297**, 556
- Houck, J. C., & Denicola, L. A. 2000, in ASP Conf. Ser. 216, Astronomical Data Analysis Software and Systems IX, Vol. 9, ed. N. Manset, C. Veillet, & D. Crabtree (San Francisco, CA: ASP), 591
- Ibragimov, A., Poutanen, J., Gilfanov, M., Zdziarski, A. A., & Shrader, C. R. 2005, *MNRAS*, **362**, 1435
- Ichimaru, S. 1977, *ApJ*, **214**, 840
- Jahoda, K., Swank, J. H., Giles, A. B., Stark, M. J., Strohmayer, T., Zhang, W., & Morgan, E. H. 1996, *Proc. SPIE*, **2808**, 59
- Kallman, T., & Bautista, M. 2001, *ApJS*, **133**, 221
- Koyama, K., et al. 2007, *PASJ*, **59**, 23
- Laurent, P., & Titarchuk, L. 2007, *ApJ*, **656**, 1056
- Maitra, D., Markoff, S., Brocksopp, C., Noble, M., Nowak, M., & Wilms, J. 2009, *MNRAS*, **398**, 1638
- Makishima, K., et al. 2008, *PASJ*, **60**, 585
- Malzac, J., Belmont, R., & Fabian, A. C. 2009, *MNRAS*, **400**, 1512
- Markoff, S., Falcke, H., & Fender, R. 2001, *A&A*, **372**, L25
- Markoff, S., & Nowak, M. 2004, *ApJ*, **609**, 972
- Markoff, S., Nowak, M., Corbel, S., Fender, R., & Falcke, H. 2003, *A&A*, **397**, 645
- Markoff, S., Nowak, M., & Wilms, J. 2005, *ApJ*, **635**, 1203
- Mayer, M., & Pringle, J. E. 2007, *MNRAS*, **376**, 435
- Miller, J. M., Homan, J., Steeghs, D., Rupen, M., Hunstead, R. W., Wijnands, R., Charles, P. A., & Fabian, A. C. 2006, *ApJ*, **653**, 525
- Miller, J. M., Wojdowski, P., Schulz, N. S., Marshall, H. L., Fabian, A. C., Remillard, R. A., Wijnands, R., & Lewin, W. H. G. 2005, *ApJ*, **620**, 398
- Mitsuda, K., et al. 2007, *PASJ*, **59**, 1
- Motta, S., Belloni, T., & Homan, J. 2009, *MNRAS*, **400**, 1603
- Noble, M. 2005, in ASP Conf. Ser. 347, Astronomical Data Analysis Software and Systems XIV, ed. P. Shopbell, M. Britton, & R. Ebert (San Francisco, CA: ASP), 237
- Nowak, M. A., Juett, A., Homan, J., Yao, Y., Wilms, J., Schulz, N., & Canizares, C. 2008, *ApJ*, **689**, 1199
- Nowak, M. A., Wilms, J., & Dove, J. B. 2002, *MNRAS*, **332**, 856
- Nowak, M. A., Wilms, J., Heinz, S., Pooley, G., Pottschmidt, K., & Corbel, S. 2005, *ApJ*, **626**, 1006
- Pottschmidt, K., Wilms, J., Nowak, M. A., Heindl, W. A., Smith, D. M., & Staubert, R. 2000, *A&A*, **357**, L17
- Pottschmidt, K., et al. 2003, *A&A*, **407**, 1039
- Poutanen, J., & Vurm, I. 2009, *ApJ*, **690**, L97
- Predehl, P., & Schmitt, J. H. M. M. 1995, *A&A*, **293**, 889
- Remillard, R. A., & McClintock, J. E. 2006, *ARA&A*, **44**, 49
- Reynolds, C. S., & Nowak, M. A. 2003, *Phys. Rep.*, **377**, 389
- Rothschild, R. E., et al. 1998, *ApJ*, **496**, 538
- Shakura, N. I., & Sunyaev, R. 1973, *A&A*, **24**, 337
- Shapiro, S. L., Lightman, A. P., & Eardley, D. 1976, *ApJ*, **204**, 187
- Shaposhnikov, N., & Titarchuk, L. 2006, *ApJ*, **643**, 1098
- Stern, B. E., Poutanen, J., Svensson, R., Sikora, M., & Begelman, M. C. 1995, *ApJ*, **449**, L13
- Stirling, A. M., Spencer, R. E., de la Force, C. J., Garrett, M. A., Fender, R. P., & Ogley, R. N. 2001, *MNRAS*, **327**, 1273
- Sunyaev, R. A., & Trümper, J. 1979, *Nature*, **279**, 506
- Takahashi, T., et al. 2007, *PASJ*, **59**, 35
- Torrejón, J. M., Schulz, N. S., Nowak, M. A., & Kallman, T. R. 2010, *ApJ*, **715**, 947
- Uchiyama, Y., et al. 2008, *PASJ*, **60**, 35
- Wilms, J., Allen, A., & McCray, R. 2000, *ApJ*, **542**, 914
- Wilms, J., Nowak, M. A., Dove, J. B., Pottschmidt, K., Heindl, W. A., Begelman, M. C., & Staubert, R. 1999, in Highlights in X-ray Astronomy, ed. B. Aschenbach & M. Freyberg (Garching: Max-Planck-Institut für extraterrestrische Physik), 98
- Wilms, J., Nowak, M. A., Pottschmidt, K., Pooley, G. G., & Fritz, S. 2006, *A&A*, **447**, 245
- Wilms, J., Pottschmidt, K., Pooley, G. G., Markoff, S., Nowak, M. A., Kreykenbohm, I., & Rothschild, R. E. 2007, *ApJ*, **663**, L97
- Xu, Y., McCray, R., & Kelley, R. 1986, *Nature*, **319**, 652
- Zdziarski, A. A., Lubinski, P., & Smith, D. A. 1999, *MNRAS*, **303**, L11